

A GAIA-PS1-SDSS (GPS1) PROPER MOTION CATALOG COVERING 3/4 OF THE SKY

HAI-JUN TIAN^{1,2}, PRASHANSA GUPTA³, BRANIMIR SESAR², HANS-WALTER RIX², NICOLAS F. MARTIN^{2,5}, CHAO LIU⁴, BERTRAND GOLDMAN^{2,5}, IMANTS PLATAIS⁶, ROLF-PETER KUDRITZKI⁷, CHRISTOPHER Z. WATERS⁷

Draft version September 26, 2017

ABSTRACT

We combine Gaia DR1, PS1, SDSS and 2MASS astrometry to measure proper motions for 350 million sources across three-fourths of the sky down to a magnitude of $m_r \sim 20$. Using positions of galaxies from PS1, we build a common reference frame for the multi-epoch PS1, single-epoch SDSS and 2MASS data, and calibrate the data in small angular patches to this frame. As the Gaia DR1 excludes resolved galaxy images, we choose a different approach to calibrate its positions to this reference frame: we exploit the fact that the proper motions of stars in these patches are *linear*. By simultaneously fitting the positions of stars at different epochs of – Gaia DR1, PS1, SDSS, and 2MASS – we construct an extensive catalog of proper motions dubbed GPS1. GPS1 has a characteristic systematic error of less than 0.3 mas yr⁻¹ and a typical precision of 1.5–2.0 mas yr⁻¹. The proper motions have been validated using galaxies, open clusters, distant giant stars and QSOs. In comparison with other published faint proper motion catalogs, GPS1’s systematic error (< 0.3 mas yr⁻¹) should be nearly an order of magnitude better than that of PPMXL and UCAC4 (> 2.0 mas yr⁻¹). Similarly, its precision (~ 1.5 mas yr⁻¹) is a four-fold improvement relative to PPMXL and UCAC4 (~ 6.0 mas yr⁻¹). For QSOs, the precision of GPS1 is found to be worse (~ 2.0 – 3.0 mas yr⁻¹), possibly due to their particular differential chromatic refraction (DCR). The GPS1 catalog will be released on-line and available via the VizieR Service and VO Service. (GPS1 is available with VO TAP Query in Topcat now, see <http://www2.mpia-hd.mpg.de/~tian/GPS1> for details)

Keywords: astrometry - catalogs - Galaxy: kinematics and dynamics - proper motions

1. INTRODUCTION

Proper motions of stars in the Milky Way, along with precise distances and radial velocities, are important pieces of observational information. In particular, they are indispensable in building the six-dimensional phase space of these stars, which in turn provides vital information for understanding the kinematics of our Galaxy (Tian et al. 2015, 2016; Liu et al. 2016).

Several comprehensive proper motion catalogs have been released over the previous decade, which have improved the depth and accuracy each time. The PPMX catalog (Röser et al. 2008) includes proper motions with a typical precision of $2 \sim 10$ mas yr⁻¹ for 18 million stars, down to a limiting magnitude of ~ 15 in r-band. The PPMXL catalog (Roeser et al. 2010) uses a combination of the United States Naval Observatory B data (USNO-B1.0; Monet et al. 2003) and Two Micron All Sky Survey (2MASS; Skrutskie et al. 2006) astrometry. It includes objects to a magnitude of $V \sim 20$, providing ~ 900 million proper motions across the entire sky, calibrated to the International Celestial Reference System (ICRS); the typical individual proper motions uncertainties range from 4 mas yr⁻¹ to more than 10 mas yr⁻¹, depending on observational history. Vickers et al. (2016) made a global correc-

tion to the proper motions in PPMXL, taking care of the fact that extragalactic sources seem to originally have non-zero proper motions in PPMXL. Zacharias et al. (2013) updated the UCAC series (Zacharias et al. 2004, 2010) and published the latest release UCAC4. This catalog contains over 113 million objects covering the entire sky, of which 105 million have proper motions complete down to about $R = 16$ mag.

Based on the Tycho-Gaia Astrometric Solution (TGAS; Michalik et al. 2015), the first data release of Gaia (Gaia DR1) published a catalog with proper motions in September 2016 for about 2 million Tycho-2 stars which only reach $G \sim 12.5$ (Høg et al. 2000; Gaia Collaboration et al. 2016a,b). Eventually, Gaia’s proper motion measurements for more than a billion stars ($G \lesssim 20.7$) in our Galaxy (de Bruijne 2012; Gaia Collaboration et al. 2016a,b) will reach a level of 5–25 μ as for $G \leq 15$ stars, superseding all the previous ground-based measurements.

While Gaia DR1 contained proper motions for only 2 million TGAS stars, it also released precise J2015.0 positions for ~ 1 billion stars across the entire sky (Gaia Collaboration et al. 2016a,b). For 90% of stars brighter than 19 mag, the positional accuracies are better than 13.7 mas, half of them are better than 1.5 mas, and some even reach 0.1 mas.

Through more than five years of surveying, Pan-STARRS1 (PS1; Chambers 2011; Magnier et al. 2017) has collected imaging data for billions of stars with high accuracy and multi-detections (> 60 on average) for each source. The average uncertainty in positions is up to ~ 10 mas for stars brighter than 19 mag in r-band.

Here we set out to combine Gaia DR1’s one-epoch position measurement at very high precision, with multi-epoch astrometry that PS1 survey provides, along with positions from SDSS and 2MASS at earlier epochs. This data set provides an unprecedented opportunity to build the best current proper

¹ China Three Gorges University, Yichang 443002, China.

² Max Planck Institute for Astronomy, Königstuhl 17, D-69117 Heidelberg, Germany. Email: hjtian@lamost.org

³ Department of Physical Sciences, Indian Institute of Science Education & Research, Mohali, Sector 81, S.A.S Nagar, Punjab 140306, India.

⁴ Key Lab for Optical Astronomy, National Astronomical Observatories, Chinese Academy of Sciences, Beijing 100012, China.

⁵ Observatoire astronomique de Strasbourg, Université de Strasbourg, CNRS, UMR 7550, 11 rue de l’Université, F-67000 Strasbourg, France.

⁶ Department of Physics and Astronomy, The Johns Hopkins University, 3400 North Charles Street, Baltimore, MD 21218, USA.

⁷ Institute for Astronomy, University of Hawaii, 2680 Woodlawn Drive, Honolulu, HI 96822, USA.

motion catalog across much of the sky.

In general, two basic approaches can be used to bring proper motions to an inertial frame: either one can use a highly accurate catalog that is already tied to the ICRS system, such as Hipparcos, and then add fainter sources to this system, as done for the Tycho-2 (Høg et al. 2000), PPMXL (Roeser et al. 2010), and UCAC4 (Zacharias et al. 2013) catalogs; or one can build a reference frame from distant extragalactic sources like galaxies (whose proper motions can be negligible), and cross-calibrate different epochs so that these sources have no proper motion. The proper motion catalog for SDSS (Munn et al. 2004) and the XPM catalog (Fedorov et al. 2009) were built using the latter method.

In this paper, we follow the second approach, and combine data from PS1, Gaia DR1, SDSS and 2MASS to obtain a catalog of proper motions dubbed GPS1. GPS1 is currently unmatched in its combination of depth, precision and accuracy among catalogs that cover a major portion of the sky. In Section 2, we detail the data sets involved. In Section 3, we lay out the approach for deriving reliable proper motions of stars from these surveys. We present our results, illustrating different data combinations, in Section 4, where we also validate the precision and accuracy of these proper motions with open clusters and distant halo stars, and make comparisons with published catalogs. We discuss possible problems that may induce small biases in proper motion estimates in Section 5. We conclude in Section 6.

Throughout the paper, we adopt the Solar motion as $(U_{\odot}, V_{\odot}, W_{\odot}) = (9.58, 10.52, 7.01) \text{ km s}^{-1}$ (Tian et al. 2015), and the IAU circular speed of the local standard of rest (LSR) as $v_0 = 220 \text{ km s}^{-1}$. Also, α^* is used to denote the right ascension in the gnomonic projection coordinate system, for example, $\mu_{\alpha^*} = \mu_{\alpha} \cos(\delta)$, and $\Delta\alpha^* = \Delta\alpha \cos(\delta)$, while ϵ denotes uncertainties, to avoid confusion with the symbol δ referring to a source’s declination. We use Δ to denote the differences in quantities such as proper motion or position.

2. DATA SET

In order to construct proper motions, we analyze and model *catalog positions* from four different imaging surveys, as discussed below. Gaia DR1 is based on observations collected between July 25, 2014 and September 16, 2015. PS1 observations were collected between 2010 and 2014. The SDSS DR9 data used here were obtained in the years between 2000 and 2008. The images from 2MASS were taken between 1997 and 2001. The characteristics of the four astrometric catalogs are summarized in Table 1.

2.1. Gaia

After the first 14 months of observation, the ESA mission Gaia published its first data release (Gaia DR1) on September 14, 2016 (Gaia Collaboration et al. 2016a,b). It consists of around 1.14 billion astrometric sources, of which only 2 million of the brightest stars contain the parallaxes and proper motions in the TGAS catalog (the so-called primary astrometric data set), while the other 1.1 billion sources have no proper motions (the so-called secondary astrometric data set). All the sources have positions and mean G-band magnitudes.

All the positions and proper motions in Gaia DR1 are calibrated to the International Celestial Reference Frame (ICRF) at epoch J2015.0. The typical uncertainty in positions and parallaxes, in the primary astrometric data set, is around 0.3 mas, while the TGAS proper motion uncertainties are around

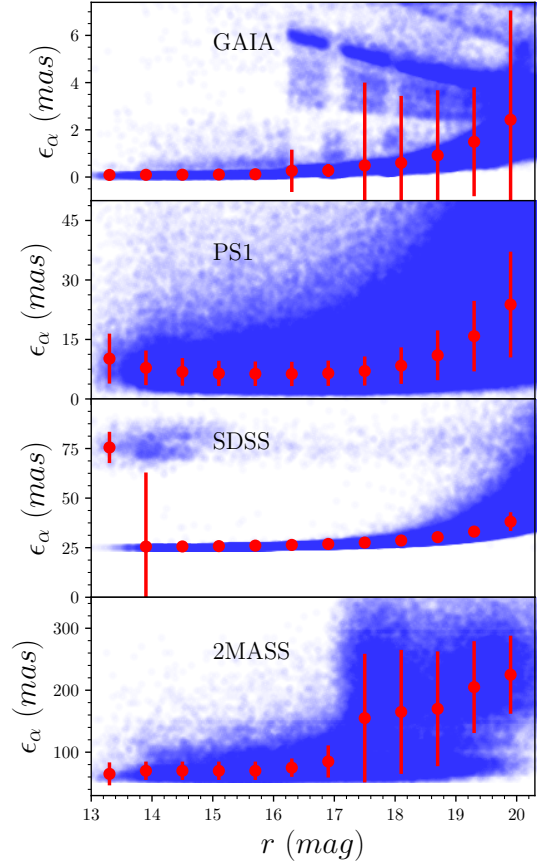


Figure 1. Precision of the source position measurements for the various data used in the construction of the GPS1 catalog, as a function of r -band magnitude. The red dots and bars indicate the average and root-mean-square (rms) of the position uncertainties in each magnitude bin. Note the dramatically different vertical axis ranges of the different panels: the formal precision of Gaia DR1 (0.31 mas/year at $14 < r < 18$) is almost two orders of magnitude higher than 2MASS’s. The PS1 precisions are about twice as good as SDSS.

1.0 mas yr^{-1} . However, the proper motions for the ~ 94000 Hipparcos stars are measured as accurate as 0.06 mas yr^{-1} . The typical uncertainty in positions in Gaia DR1’s secondary astrometric data set is $\sim 7 \text{ mas}$, as shown in the top panel of Figure 1. Note that $\sim 99.7\%$ sources in Gaia DR1 are in the magnitude range of $11.2 < G < 21$, as the saturating and limiting magnitudes are $G \sim 12$ and 20.7 , respectively (Gaia Collaboration et al. 2016a).

2.2. Pan-STARRS1

Pan-STARRS1 (PS1; Chambers 2011) is a wide-field optical/near-IR survey telescope system, located at the Haleakala Observatory on the island of Maui in Hawaii. It has been conducting multi-epoch and multi-color observations over the entire sky visible from Hawaii ($\text{Dec} \gtrsim -30^\circ$). PS1 imaged in five bands $g_{P1}, r_{P1}, i_{P1}, z_{P1}, y_{P1}$, with a 5σ single epoch depth of 22.0, 22.0, 21.9, 21.0 and 19.8 magnitude, respectively. The average wavelengths of its five filters are 481, 617, 752, 866, and 962 nm, respectively (Stubbs et al. 2010; Tonry et al. 2012). Unlike SDSS, PS1 observations in different bands are not taken simultaneously, and the wavelength coverage of the filters is also different. Roughly 56% of the PS1 telescope observing time was dedicated to the PS1 3π survey, which planned to observe each position 4 times per filter over 5 years. Throughout the 5 years, from 2010 to 2014, the PS1 3π survey imaged a sky area of $\sim 30,000 \text{ deg}^2$

Table 1
Characteristics of the four astrometric catalogs that constitute GPS1

Survey	Sky Coverage	Limiting Magnitude	Saturating Magnitude	Positional Uncertainty	Epochs	Average Detections
		mag		mas		
Gaia DR1	4π	$G \sim 20.7$	$G \sim 11.2$	~ 7	2015.0	1
PS1 PV3	3π	$r_{P1} \sim 22.0^a$	$r_{P1} \sim 13.5$	~ 15	2010-2014	65 ^d
SDSS DR9	π	$r \sim 23.1^a$	$r \sim 14.1$	~ 25	2000-2008	1
2MASS	4π	$K_s \sim 14.3^b$	$K_s \sim 8^c$	~ 100	1997-2001	1

^a The limiting magnitude for detection with $S/N = 5$.

^b The limiting magnitude for detections with $S/N = 10$.

^c The saturating magnitude for detections in 1.3 s exposure time.

^d The catalog of PS1 PV3, on an average, includes 65 detections for each source in ~ 5 seasons.

in 65 epochs. Images are automatically processed using the survey pipeline (Magnier et al. 2008, 2017) that performs bias subtraction, flat fielding, astrometry, photometry, as well as image stacking and differencing. The photometric calibration of the survey is ~ 0.01 mag (Schlafly et al. 2012).

All data processing shown here was carried under PS1 catalog Processing Version 3 (PV3; Chambers et al. 2016). We stored the catalog locally in the Large Survey Database (LSD) format (Juric 2012), which allows for a quickly and efficient manipulation of very large catalogs ($> 10^9$ objects). The stored catalog contains both the point-spread function (PSF) and aperture photometry for each object, whose difference provides a convenient parameter for separating stars from background galaxies.

2.2.1. Season Average and Positional Uncertainty in PS1

The average number of total detections per PS1 source is 65, over 5.5 years. Each source is detected typically more than ten times in an observing season. We determine a robust average position and its uncertainties for each object within a season (hereafter, SeasonAVG). The typical single-epoch positional precision of bright ($r_{PS1} < 19.0$) sources is ~ 10 mas, as illustrated in the second panel of Figure 1.

2.2.2. PS1 Astrometry Outlier Cleaning

A comparison of position measurements among PS1 repeat observations for a sample of sources, shows that some estimates strongly deviate from the median position, and hence must be outliers. To remove them, we apply selection cuts on (1) individual detections, and on (2) individual objects:

- select detections for whom 85% of their PSF lands on good CCD pixels ($psf_qf > 0.85$);
- remove detections with bad photometry ($photo_flag \& 4027825560 = 0$), since problems that affect the PSF photometry also frequently affect the astrometry;
- remove detections that deviate by more than 3 times the robust rms scatter from their median values, where the robust rms is defined as $0.741 \times (75^{th} \text{ percentile} - 25^{th} \text{ percentile})$ (Lupton 1993);
- keep objects with at least three 'good' detections;
- calculate the season-averaged position of PS1 astrometry (SeasonAVG), and its uncertainty from 'good' detections;
- keep objects with at least three SeasonAVG measurements.

After the above filtering of the PS1 catalog, we keep 350 million objects with billions of detections.

2.3. SDSS

The Sloan Digital Sky Survey (SDSS) used a dedicated 2.5-meter wide-field telescope (Gunn et al. 2006) for imaging over roughly one third of the Celestial Sphere. The imaging was performed simultaneously in five optical filters: u , g , r , i and z with central wavelengths of about 370, 470, 620, 750 and 890 nm, respectively (Gunn et al. 1998; Fukugita et al. 1996). Stellar objects were uniformly reduced by the photometric pipeline. The $S/N = 5$ limiting magnitudes are 22.1, 23.2, 23.1, 22.5 and 20.8 mag (AB system) in the five band-passes, respectively. And stars saturate at 12.0, 14.1, 14.1, 13.8, and 12.3 mag in these same five bands. (Gunn et al. 1998)

Since its regular operations began in 2000 April, SDSS has gone through a series of stages: SDSS-I (York et al. 2000), which was in operation through 2005, focused on a 'Legacy' survey of five-band imaging and spectroscopy of well-defined samples of galaxies and QSOs, SDSS-II operated from 2005 to 2008, and finished the Legacy survey, followed by SDSS-III. For our purposes, only the photometric data is relevant, especially the SDSS-I photometric sources which were imaged in the early epochs.

The typical astrometric uncertainties for bright stars ($r < 19.0$ mag) are around 20-30 mas per coordinate (Stoughton et al. 2002), as shown in the third panel of Figure 1.

While individual SDSS measurements are a factor of 2-3 less precise than PS1, the long epoch baseline makes this data very valuable.

2.4. 2MASS

Two Micron All Sky Survey (2MASS; Skrutskie et al. 2006), was conducted from two 1.3 m diameter dedicated telescopes located in the southern and northern hemisphere, which collected 25.4 terabytes of raw imaging data in the near-infrared $J(1.25 \mu m)$, $H(1.25 \mu m)$, and $K_s(1.25 \mu m)$ band-passes, covering virtually the entire celestial sphere between June 1997 and February 2001. The 2MASS All-Sky Data Release identifies around 471 million point sources, and 1.6 million extended sources. The limiting magnitudes at $S/N = 10$ are $J = 15.8$, $H = 15.1$, and $K_s = 14.3$, and point sources saturate at $K_s = 8$ magnitude for less than 1.3 s exposure time.

Bright source extractions have 1σ photometric uncertainty of less than 0.03 mag and the astrometric accuracy is of the order 100 mas, as shown in the bottom panel of Figure 1. Because of large positional uncertainties, 2MASS positions provide only a weak constraint for proper motion measurements.

3. DERIVATION OF PROPER MOTIONS

The basic premise of our analysis is that the cataloged object coordinates, at any given epoch, are precise relative coord-

dinates of objects within a small angle on the sky (say, $\sim 1^\circ$). Yet, their absolute astrometry (i.e. the coordinates' *accuracy*) cannot be trusted across epochs and surveys. But all the ground-based imaging surveys are deep enough to contain a large number of compact or symmetrical galaxies with well-measured centroids, for which the proper motions should effectively be zero. We use those sources to bring the epochs to the same reference frame (see, e.g. Munn et al. 2004). While the Gaia imaging is of course deep enough to contain many galaxies, the positions of resolved objects have not yet been released in DR1. Therefore, we need a variant of the above procedure to bring the ground-based data and Gaia DR1 to the same local reference frame.

3.1. Qualitative Overview: Reference Frame Alignment and Proper Motion Fitting

We give a brief summary of all the steps that lead to the construction of the proper motion catalog. For practical reasons, we consider different sub-areas of the sky in the course of this alignment: a 'tile' in this paper is an area of constant size of 10° by 10° , a 'patch' is a smaller region with area 1° by 1° , and the 'pixel' is the smallest region with area ~ 12 arcmin².

1. Select a tile of the sky and acquire all its objects from PS1, Gaia, 2MASS, and SDSS (if it covers this region) databases.
2. Classify the objects as stars and galaxies.
3. Separate the tile into equal-area pixels using the HEALPix system (Calabretta & Roukema 2009) with 10 levels (i.e. $N_{SIDE} = 10$), and label each pixel with its center position, namely, the Anchor Point (AP).
4. Construct a reference catalog by averaging repeatedly observed positions of PS1 galaxies in this tile.
5. Cross-match the PS1 objects with Gaia, 2MASS and SDSS using a $1.5''$ search radius.
6. For each observing epoch, calculate the mean positional offset of galaxies relative to their reference position.
7. Correct the positions of stars to the reference frame, assuming that their offset is the same as that of galaxies, in the same pixel and MJD.
8. To measure a proper motion of a star, fit a straight line (in the least squares sense) to PS1 SeasonAVG, 2MASS, and SDSS positions (if existing), where the positions are weighted by their inverse variance (the parallax is neglected).
9. Use the information from Step 8. to predict the stars' position at the Gaia epoch (2015.0). Then calculate the mean offset within a sky pixel between the stars' predicted positions and those of Gaia DR1.
10. Use the offset from Step 9. to bring the Gaia observations to the common reference frame.
11. Similar to Step 8. fit the PS1 SeasonAVG, Gaia, 2MASS, and SDSS positions to get the final proper motion for each star.

The following subsections detail the main steps in the above procedure.

3.2. Reference and Astrometric Calibration

We now elaborate more on the steps to bring the cataloged positions to a common reference frame before fitting for proper motions.

3.2.1. Sky-Direction Dependence of the Astrometric Offsets among Different Epochs

We do not know *a priori* on what angular scales the positional offsets vary between different surveys and epochs. This must be determined from the data itself. Using PS1 data at relatively low Galactic latitudes, we investigate the positional offsets of galaxies in different epochs, and find prominent offset patterns in different directions and epochs. Covering a sizable portion of the sky, Figure 2 represents the median offsets among PS1 cataloged galaxy positions (the left column), along with the *rms* of the individual object's offsets (the middle column), and the galaxy numbers in each patch (the right column). The median and *rms* of the offsets are obtained from all galaxies with at least three detections. The black solid and two dashed lines correspond to the locations with Galactic latitude $b = 0^\circ$, -20° , and 20° , respectively. Different epochs of the same area in the sky are presented in the different panel rows. The offset and *rms* patterns remain unchanged if the patch size were changed to 0.5° by 0.5° ; this leads us to choose 1° as a radius to select background galaxies and use them to do the following calibration.

We then take these median offsets in α and δ , and add them to positions of PS1 stars at a given epoch and in the current sky pixel. This is done separately for each sky pixel and different PS1 epochs. The single-epoch positions from 2MASS and SDSS are calibrated using the same procedure.

The procedure described above requires careful identification of galaxies. We define galaxies as objects for which the differences between point spread function (PSF) and aperture magnitudes in PS1 r_{P1} and i_{P1} bands lie between 0.3 and 1.0 mag. Using PS1 photometry in a field near M67, we can investigate how well this criterion works to selected galaxies. Sources in the field of M67 were observed and spectroscopically well classified by SDSS, and we take these classifications as the ground truth. Figure 3 displays the distribution of point and extended sources in the panel of $m_{psf} - m_{ap}$ v.s. m_{psf} in r_{P1} -band. The black dots are the sources from PS1 which include point and extended objects. The red points are the SDSS galaxies. The blue points are the galaxy candidates identified with the magnitude differences ($m_{psf} - m_{ap}$), which lies between 0.3 mag and 1.0 mag in both the r_{P1} and i_{P1} bands. By cross-matching with SDSS galaxies, we estimate the success fraction ($r_{success}$) of galaxy selection in different magnitude bins. The success fraction can reach up to 99% for faint sources ($r_{psf} > 17$ mag), as shown in the right sub-panel of Figure 3. This result indicates that galaxy selection criterion works fine for the selection of faint galaxies. In practice, the galaxies used to build the reference catalog in this work are dominated by faint galaxies. The galaxy candidates (blue dots) have higher contaminations at the bright end, mainly because of the image saturation. Even so, it is still safe to do the positional calibration using the median offset of hundreds of galaxies.

As Gaia's DR1 does not contain galaxies, we bring the Gaia positions to the common reference system, exploiting the fact that the proper motions of (almost) all stars are effectively linear. We use proper motions of bright stars ($14.5 < m_r < 17.5$) measured using PS1, 2MASS, and SDSS positions to predict

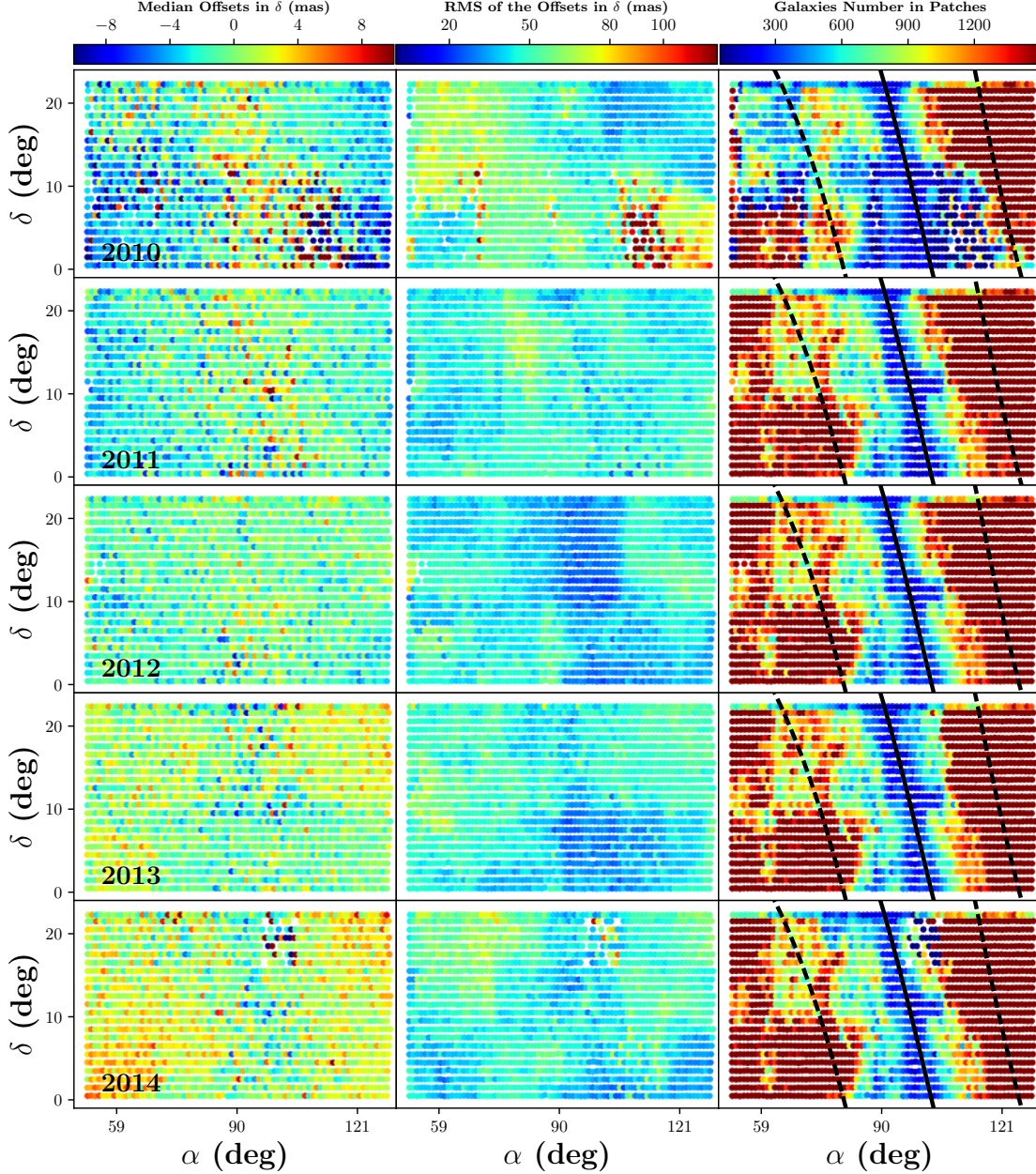


Figure 2. Sample maps of the position offsets between individual PS1 epochs and the mean reference positions, as a function of directions on the sky, shown for different epochs as different rows in the left column. The corresponding *rms* of positional offsets are shown in the middle column, and the galaxy numbers used to determine the offset within each patch are shown in the right column. The median and *rms* of the offset for each patch are obtained from the positional residuals of all the galaxies within a patch relative to their median measurement of at least 3 epochs. Most of the patches include more than 600 galaxies, except for some regions close to the Galactic plane. The black lines in the right column mark the sky direction of $b = 0^\circ$ (solid line) and $b = \pm 20^\circ$ (dashed lines).

the positions of the same stars at the epoch of Gaia observations (i.e., 2015.0). For the nearest 100 stars to each AP, we then take the median difference between Gaia’s cataloged positions and the predicted reference frame positions at the given MJD. This offset is then subtracted from the Gaia positions of all stars located in that sky pixel.

We use simulations to validate this procedure for bringing the Gaia DR1 positions to our reference frame. We choose around 2000 stars from the PS1 catalog, and calculate their proper motions from PS1 detections. Using these proper motions, we predict the position of each star at Gaia’s epoch, and record the positions as true locations of the simulated Gaia

data. We divide the sky region into small equal-area patches. For each patch, we generate a random positional offset between -10 mas and 10 mas and assign the offset to each simulated Gaia star located in the same patch. For each star, we generate an additional random observational error ($\sigma = 3.0$ mas). Finally, we calibrate the ‘observed’ Gaia stars with the nearby 20 stars, and calculate the differences between the true and calibrated positions. The median of the differences is around zero, and *rms* is smaller than 1.5 mas.

3.2.2. Magnitude and Declination Dependent Offset Patterns

Even after these corrections, the differences between the PS1 reference positions and (corrected) Gaia DR1 positions

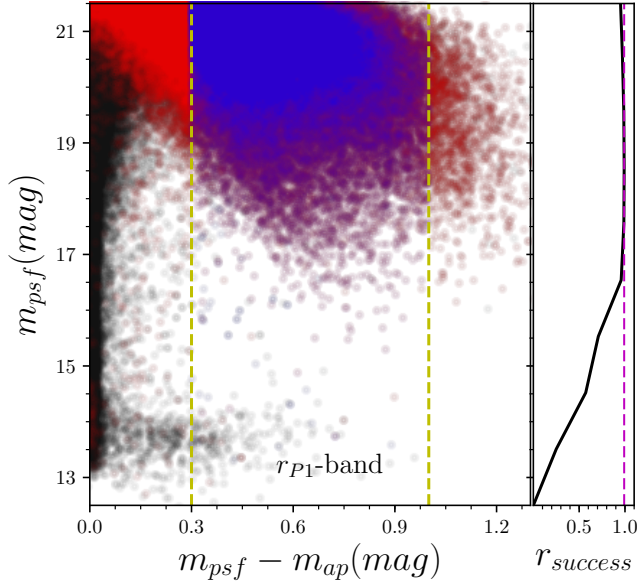


Figure 3. The distribution of point and extended sources distribution in the plane of $m_{psf} - m_{ap}$ v.s. m_{psf} in r_{P1} -band. Here, m_{psf} and m_{ap} are the PSF and aperture magnitudes, respectively. The figure illustrates star - galaxy separation with PS1 photometry in the field of M67, used to identify the galaxy sample for creating (and calibrating to) the position reference frame. The blue dots denote the galaxy candidates used for building the reference catalog, selected by $0.3 \leq m_{psf} - m_{ap} \leq 1$ in both PS1 r_{P1} and i_{P1} (the borderlines are marked with the two yellow dashed lines). The red dots are galaxies identified by SDSS, which are assumed to be true galaxies. The black dots are the sources including point and extended sources. The right sub-panel displays the successful ratio ($r_{success}$) of this galaxy selection criterion. The ratio is obtained by cross-matching PS1 galaxy candidates (blue dots) and SDSS galaxies (red dots). This star-galaxy separation works very well for $m > 16$, and the ratio can reach up to 99% (marked with the magenta dashed line).

show some dependence on other quantities, namely, on declination and magnitude of the source. Figure 4 shows the variation of the mean positional offsets with r-band magnitude, both at high (the left panels) and low (the right panels) declinations. The positional offset for each star is obtained by taking the difference of the Gaia’s predicted position and the originally observed position. The predicted position for each star is calculated from the PS1, SDSS, and 2MASS fitted proper motion. The black dashed lines are the locations of the median offsets with $14.5 < m_r < 17.5$, which mark the zero-point difference between Gaia and PS1-based reference. The red dots and bars are the median offsets and uncertainties in different magnitude bins, and they show obvious variations with magnitude. In particular the high and low declination variations in the direction of δ (the bottom panels) are almost opposite, while in the direction of α (the top panels) the offsets keep roughly constant. Irrespective of the origin of this offset pattern, it must be removed or mitigated. To do so, we build a relation model between the offset and magnitude on a larger angular scale, i.e., for each star tile. For most tiles, the offset is roughly linear with magnitude,

$$\Delta(\delta, m) = c \cdot m - \Delta(\delta, m_0), \quad (1)$$

where $\Delta(\delta, m_0)$ is the zero-point difference between the Gaia and PS1-based reference at a given declination (the dashed lines in Figure 4), m_0 is the average magnitude of stars with $14.5 < m_r < 17.5$ (since we use the stars in this magnitude bin to place Gaia positions onto the PS1 reference frame), and c is the slope of the offset line. In practice, one could also

remove the magnitude dependent offset for each star by linear interpolation between the magnitudes and offsets.

While we have been able to correct for this effect, we have not been able to identify its root cause with any certainty. It seems plausible that it can be traced to the PS1’s experimental set-up: it is known that the cataloged PS1 positions have had some magnitude dependence (Koppenhöfer & Henning 2011), and the differential chromatic refraction (DCR) (Kaczmarczik et al. 2009) may be imperfectly corrected. This issue will be discussed further in Section 5.3. This type of offset is also detected in SDSS, but at a much lower level (< 5 mas). The offset in SDSS positions does not significantly affect the final proper motion measurement as its is much smaller than the average positional uncertainty in SDSS positions (~ 25 mas).

3.3. Proper Motion Fitting

After calibrating the cataloged positions for each object in five (or six) PS1 epochs, one Gaia epoch, one 2MASS epoch, and possibly one SDSS epoch onto the same reference frame, we can calculate the proper motion for each star by performing a linear least squares fit to positions observed at up to nine different epochs. We do this by using a simple χ^2 fit that includes outlier rejection. We start with

$$\chi^2 = \sum_i^N \frac{[\hat{y}_i^o - y_i^{model}(t_i)]^2}{\epsilon_i^2}, \quad (2)$$

where \hat{y}_i^o is the observed position of a star at epoch i , and ϵ_i the position uncertainty. All the positional uncertainties consist of two parts: one part is the individual position precision, illustrated in Figure 1; and the other part is the uncertainty from the offset calibration, illustrated for PS1 in Figure 2. $y_i^{model}(t_i)$ is the predicted position by a linear model at the given time t_i , N is the number of epochs in different surveys. The position \hat{y}_i^o has been calibrated by

$$\hat{y}_i^o = y_i^o - \Delta_i(\alpha, \delta) - \Delta_i(\delta, m), \quad (3)$$

where y_i^o is the original cataloged position of a star at epoch i , $\Delta_i(\alpha, \delta)$ is the direction dependent offset described in Section 3.2.1, and $\Delta_i(\delta, m)$ is the magnitude and declination dependent offset described in Section 3.2.2.

Unrecognized outliers in positional data may induce a spurious proper motion estimate. In order to remove such outliers, we employed leave-one-out cross-validation. We withhold one of the observation epochs, fit a straight line to the remaining positions, and calculate the reduced χ_ν^2 ($\equiv \chi^2 / (N_{data\ points} - 2)$). This procedure is repeated for each observation epoch, and we adopt the fit with the minimum χ_ν^2 . In practice, leave-one-out fits can eliminate outliers efficiently. The left subplot in Figure 5 represents a typical SeasonAVG outlier (the second red point), which severely affects the proper motion fitting, as shown by the red dashed line.

Even though Gaia DR1 contributes only one epoch, precisely anchoring down the position at that one epoch can significantly reduce the proper motion uncertainties. For example, the red solid line in the left subplot of Figure 5 illustrates the proper motion (-8.66 ± 1.73 mas yr $^{-1}$) by fitting the 4 PS1 SeasonAVG points (the red dots, excluding the outlier) and 1 Gaia point (the yellow dot). The uncertainty of the proper motion is reduced by ~ 1.36 mas yr $^{-1}$, compared to the fit based on PS1-only, represented by the red dashed line.

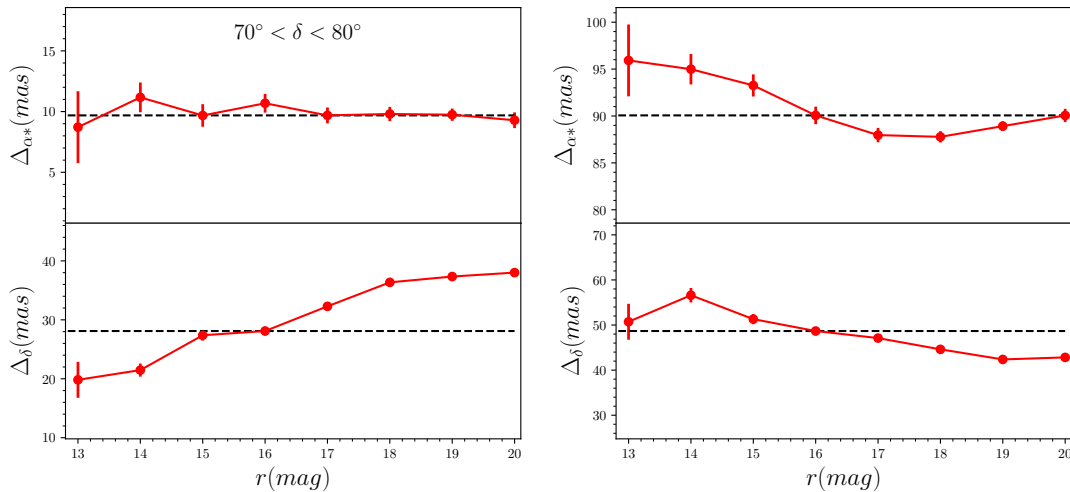


Figure 4. The position offsets between Gaia and PS1 reference positions depend both on magnitude and on declination: high declinations ($70^\circ < \delta < 80^\circ$) are shown in the left panel and low latitudes in the right panel ($-30^\circ < \delta < -20^\circ$). The black dashed lines are the locations of median offsets with $14.5 < m_r < 17.5$ mag, which mark the zero-point difference between Gaia and PS1-based reference. The red dots and bars are the median offsets and uncertainties in different magnitude bins. While the source of these trends presumably lies with the PS1 data, operationally we correct the Gaia positions to the PS1 reference positions, as we are only concerned with proper motions here.

The typical positional uncertainty of SDSS is around 25 mas for objects brighter than 19 mag, an order of magnitude worse than Gaia. Yet, the long epoch-baseline of SDSS makes these data important for the proper motion fit. The black point in the right hand panel of Figure 5 is a position observed by SDSS about 15 years ago. The proper motion ($-8.93 \pm 1.19 \text{ mas yr}^{-1}$) represented by the red solid line is obtained by fitting the 4 SeasonAVG points (the red dots, excluding the outlier), 1 Gaia point (the yellow dot), 1 SDSS point, and 1 2MASS point (the magenta dot), simultaneously. Compared to $-4.33 \pm 3.09 \text{ mas yr}^{-1}$ (only PS1), the uncertainty is reduced by $\sim 1.9 \text{ mas yr}^{-1}$; including the 2MASS point actually improves only by $\sim 0.05 \text{ mas yr}^{-1}$. Besides improving the individual objects' precision, the SDSS and Gaia points also enhance the accuracy of the proper motion. Wherever SDSS is available, the 2MASS point contributes little weight because of its large positional errors (on average $> 100 \text{ mas}$ for objects brighter than 20 mag).

The blue points in the right-panel of Figure 5 show the 64 individual detections from PS1 (as opposed to the seasonAVG points). These points have been cleaned of outliers by the cuts described in Section 2.2.2. The blue solid line (proper motion = $-8.63 \pm 0.81 \text{ mas yr}^{-1}$) is obtained by fitting 67 points (64 individual PS1, 1 SDSS, 1 Gaia, and 1 2MASS) simultaneously, consistent within 1σ with the red line (by fitting 4 SeasonAVG, 1 SDSS, 1 Gaia, and 1 2MASS points). The positional uncertainty cannot be estimated straightforwardly for any one individual detection. Therefore, we used a simple empirical model to assign the positional uncertainty for each star according to its magnitude,

$$\sigma_{(\alpha,\delta)}(\text{mas}) = \sqrt{15^2 + (1000 \times \epsilon_{m_r})^2}, \quad (4)$$

where ϵ_{m_r} is the r -band magnitude error in the individual detection. This formula can model the relation between observational uncertainty and magnitude, but cannot well discriminate among uncertainties for the same object in different detections. Therefore, the modeled observational uncertainty cannot qualify as weight in the proper motion fitting procedure. That means, the precision (0.81 mas yr^{-1}) of the proper motion obtained by fitting the blue points is unreliable.

For comparison, the proper motions from other catalogs

for the star in the fitting example are displayed in Figure 5. The green dashed line is the proper motion estimate ($-8.79 \pm 1.26 \text{ mas yr}^{-1}$) from Fritz & Kallivayalil (2015). The proper motions fitted with either seasonAVG (the red solid line) or the PS1 individual points (the blue solid line) agree well in this case. The black dashed line is the proper motion estimate ($-11.22 \pm 1.85 \text{ mas yr}^{-1}$) from the PS1 PV3 catalog, combining the PS1 individual points with 2MASS. This proper motion is larger than others, possibly because higher weight is assigned to the 2MASS point for the proper motion fit in PV3 catalog. Among these different proper motion estimates, the fit using seasonAVG positions turned out to be best. It appears accurate and is easy to fit, and we adopt the seasonAVG fit mode for all the stars in the GPS1 construction.

3.4. Cross-validation of the PS1 Position Uncertainties

We can use cross-validation to test whether the PS1 SeasonAVG position uncertainties are realistic. To do so, we randomly choose 2000 bright stars ($14.5 < m_r < 17.5$) from PS1 and take the difference between the observed SeasonAVG PS1 position in a season, and the value predicted for that season by the proper motion fit where that particular season has been withheld. Figure 6 shows the histogram of the residuals for the sample, normalized with the uncertainty in the PS1 SeasonAVG position, i.e., $\hat{\Delta}_\delta = (\delta_o - \delta_p) / \epsilon_\delta$, where ϵ_δ is the uncertainty of position, δ_o and δ_p are the observed and predicted PS1 SeasonAVG positions, respectively.

Ideally, the width of the histogram should be unity, but it is ~ 1.58 . Tests on mock data have shown that the cross-validation systematically overestimates the deviations, when the number of data points in a proper motion fit is small (< 10 points) in the simulation. For example, even though the true astrometric uncertainty in a mock sample was set to 5 mas, the cross-validation analysis returned the uncertainty of 7 mas.

Thus, we can conclude that the PS1 SeasonAVG uncertainties are realistic within a factor of 1.5.

4. RESULTS AND PERFORMANCE

Using the approach described in Section 3, we determine proper motions for around 350 million stars, to magnitude of

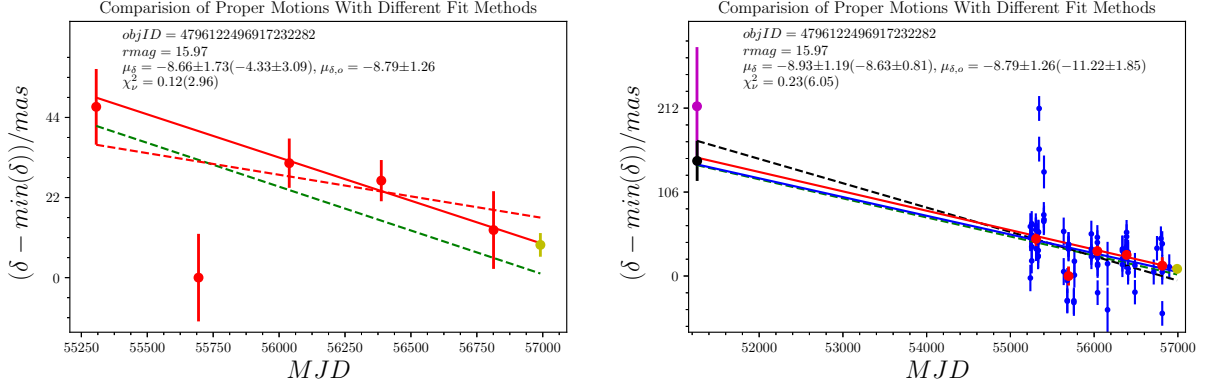


Figure 5. Illustration of the different options in proper motion fitting, using the various combinations of data sets, and outlier rejection. The left panel shows fits to the combination of the Gaia (yellow) and PS1 SeasonAVG data (red). The red point at MJD \sim 56800 in the PS1 SeasonAVG data is an obvious outlier. The red solid line shows the proper motion estimate, -8.66 ± 1.73 mas yr $^{-1}$, after removing one PS1-season outlier and including the Gaia DR1 (yellow) point. The red dashed line shows the analogous estimate, -4.33 ± 3.09 mas yr $^{-1}$, when fitting all five PS1 epochs, including the outlier, but without the Gaia DR1 epoch. In the right panel, the red solid line (proper motion: -8.93 ± 1.19 mas yr $^{-1}$, 4 PS1 SeasonAVG excluding the outlier) and blue solid line (proper motion: -8.63 ± 0.81 mas yr $^{-1}$, 64 PS1 individual blue points) are drawn by fitting the combination of Gaia (yellow dot), PS1, SDSS (black dot), and 2MASS (magenta dot). The black dashed line (for comparison) on the right is plotted according to the proper motion (-11.22 ± 1.85 mas yr $^{-1}$) from PS1 PV3 catalog. The green lines in both panels are according to the proper motion (-8.79 ± 1.26 mas yr $^{-1}$) from by Fritz & Kallivayalil (2015). The fitting is taken on a same star example in the left and right panels.

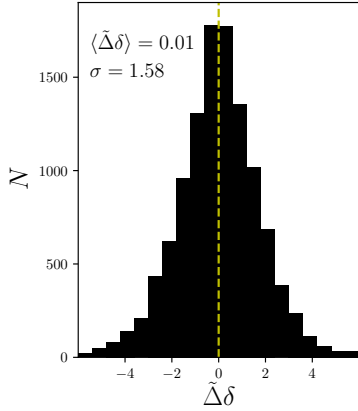


Figure 6. The histogram of the normalized residuals obtained from the cross-validation, to check the uncertainties of PS1 SeasonAVG positions. The dashed yellow line marks the zero location.

~ 20 in r-band. The catalog draws on PS1 SeasonAVG and Gaia DR1 as the primary data, together with the best available combinations of other surveys. The final catalog uses the robust fit (where all the data points are fitted regardless of outliers), and cross-validation fit (where outliers are removed while fitting). For reference, we also include a fit without Gaia and one with only PS1 SeasonAVG points. Table 2 lists the main columns contained in the catalog. In the following sub-sections, we discuss the precision and accuracy of proper motions in different cases.

4.1. Uncertainties in Proper Motions

The footprint overlap among Gaia, PS1, SDSS and 2MASS surveys introduces some complexity: $\sim 23\%$ stars are covered by Gaia, PS1, and SDSS, $\sim 73\%$ by PS1 and Gaia, but not SDSS, $\sim 3\%$ stars are only observed by PS1. Therefore, it is necessary to investigate how the final proper motions are affected by combining different data sets.

4.1.1. The Different Data Set Combinations

We now investigate how the uncertainties in proper motion differ among the following four combinations of data sets:

Gaia + PS1 + SDSS + 2MASS (GPS), Gaia + PS1 + 2MASS (GP), PS1 + SDSS + 2MASS (PD), and *only* PS1 (PS1). For the catalog table, different surveys are assigned different integer identifiers: 0, 5, 10, and 20 for PS1, 2MASS, SDSS, and Gaia, respectively. This defines a *flag* for different survey combinations entering a fit, represented as the sum of the individual survey identifiers. The primary observations are those from PS1, so the positions for each star must include the PS1 detections when fitting for proper motion.

Figure 7 summarizes the distribution of proper motion uncertainties for the four different combinations. In the four panels, the blue points correspond to the 50,000 stars randomly selected from the sky and the red curves are the median uncertainties in proper motions within different magnitude bins. The average uncertainties in magnitude bins are listed in Table 3, with the mean ($14 < m_r < 18$) marked by black lines. In the GPS mode (see Table 3), the average uncertainties are $\epsilon_{\mu_{\alpha^*}} \sim 1.35$ mas yr $^{-1}$ and $\epsilon_{\mu_{\delta}} \sim 1.21$ mas yr $^{-1}$. This is slightly better than the GP mode ($\mu_{\alpha^*} \sim 1.41$ mas yr $^{-1}$ and $\mu_{\delta} \sim 1.23$ mas yr $^{-1}$). Without Gaia positions (PD mode), the typical uncertainties become $\epsilon_{\mu_{\alpha^*}} \sim 1.91$ mas yr $^{-1}$ and $\epsilon_{\mu_{\delta}} \sim 1.72$ mas yr $^{-1}$. Gaia positions improve the precision by ~ 0.6 mas yr $^{-1}$ for both the $\epsilon_{\mu_{\alpha^*}}$ and $\epsilon_{\mu_{\delta}}$. For PS1 data alone, the mean uncertainties become $\epsilon_{\mu_{\alpha^*}} \sim 2.53$ mas yr $^{-1}$ and $\epsilon_{\mu_{\delta}} \sim 2.12$ mas yr $^{-1}$. The precision improvement is dominated by Gaia (~ 1.0 mas yr $^{-1}$ on an average).

For the brighter stars with $m_r < 14$, the proper motion uncertainties increase as the PS1 detections begin to saturate. A comparison of the GP mode with the PS1 mode reveals that Gaia can improve the precision of the bright stars by ~ 2.1 mas yr $^{-1}$, as shown in Table 3. Comparing with the PS1 mode, we find that SDSS in the PD mode can improve the uncertainty by ~ 1.1 mas yr $^{-1}$. Therefore, Gaia detections are also more effective in reducing uncertainties than SDSS for the case of bright stars with $m_r < 14$.

For the fainter stars with $m_r > 18$, the positional uncertainties are worse than those of brighter stars, implying that the precision of the obtained proper motions will be worse towards the faint end. As the values in Table 3 show, both SDSS and Gaia can improve the precision of the proper mo-

Table 2
The columns of GPS1 catalog

Column	Unit	description	
1	obj_id ^a	-	The unique but internal object_id in PS1
2	ra	degree	Right ascension at J2015.0 from Gaia DR1
3	dec	degree	Declination at J2015.0 from Gaia DR1
4	e_ra	mas	Positional uncertainty in right ascension at J2015.0 from Gaia DR1
5	e_dec	mas	Positional uncertainty in declination at J2015.0 from Gaia DR1
6	ra_ps1	degree	Average right ascension at J2010 from PS1 PV3
7	dec_ps1	degree	Average declination at J2010 from PS1 PV3
8	pmra	mas yr ⁻¹	Proper motion with robust fit in $\alpha \cos \delta$
9	pmde	mas yr ⁻¹	Proper motion with robust fit in δ
10	e_pmra	mas yr ⁻¹	Error of the proper motion with robust fit in $\alpha \cos \delta$
11	e_pmde	mas yr ⁻¹	Error of the proper motion with robust fit in δ
12	chi2pmra	-	χ^2_{ν} from the robust proper motion fit in $\alpha \cos \delta$
13	chi2pmde	-	χ^2_{ν} from the robust proper motion fit in δ
14	pmra_x	mas yr ⁻¹	Proper motion with cross-validated fit in $\alpha \cos \delta$
15	pmde_x	mas yr ⁻¹	Proper motion with cross-validated fit in δ
16	e_pmra_x	mas yr ⁻¹	Error of the proper motion with cross-validated fit in $\alpha \cos \delta$
17	e_pmde_x	mas yr ⁻¹	Error of the proper motion with cross-validated fit in δ
18	pmra_ng	mas yr ⁻¹	Proper motion with no Gaia robust fit in $\alpha \cos \delta$
19	pmde_ng	mas yr ⁻¹	Proper motion with no Gaia robust fit in δ
20	e_pmra_ng	mas yr ⁻¹	Error of the proper motion with no Gaia robust fit in $\alpha \cos \delta$
21	e_pmde_ng	mas yr ⁻¹	Error of the proper motion with no Gaia robust fit in δ
22	pmra_ps	mas yr ⁻¹	Proper motion with only PS1 robust fit in $\alpha \cos \delta$
23	pmde_ps	mas yr ⁻¹	Proper motion with only PS1 robust fit in δ
24	e_pmra_ps	mas yr ⁻¹	Error of the proper motion with only PS1 robust fit in $\alpha \cos \delta$
25	e_pmde_ps	mas yr ⁻¹	Error of the proper motion with only PS1 robust fit in δ
26	chi2pmra_ps	-	χ^2_{ν} from only PS1 robust fit in $\alpha \cos \delta$
27	chi2pmde_ps	-	χ^2_{ν} from only PS1 robust fit in δ
28	n_obsps1	-	The number of SeasonAVG observations used in the proper motion fit
29	n_obs	-	The number of all the observations used in the robust proper motion fit
30	flag ^b	-	An integer number used to flag the different data combination in the proper motion fit.
31	magg	mag	g-band magnitude from PS1
32	magr	mag	r-band magnitude from PS1
33	magi	mag	i-band magnitude from PS1
34	magz	mag	z-band magnitude from PS1
35	magy	mag	y-band magnitude from PS1
36	e_magg	mag	Error in g-band magnitude from PS1
37	e_magr	mag	Error in r-band magnitude from PS1
38	e_magi	mag	Error in i-band magnitude from PS1
39	e_magz	mag	Error in z-band magnitude from PS1
40	e_magy	mag	Error in y-band magnitude from PS1
41	maggaia	mag	G-band magnitude from Gaia
42	e_maggaia	mag	Error in G-band magnitude from Gaia

^a Here objID is an internal PS1 ID, which is different from the public ID released in PS1 catalog.

^b In order to label the different survey combinations for proper motion fit, we assign PS1, 2MASS, SDSS, and Gaia with different integer identifiers, i.e. 0, 5, 10, and 20, respectively, and define a *flag* with the sum of identifiers of surveys combined.

Table 3
The formal fitting uncertainties of the proper motions in the different data combinations

ID	Mode	$m_r < 14$		$14 < m_r < 18^a$		$m_r > 18$		N^b
		$\langle \epsilon_{\mu_{\alpha*}} \rangle$	$\langle \epsilon_{\mu_{\delta}} \rangle$	$\langle \epsilon_{\mu_{\alpha*}} \rangle$	$\langle \epsilon_{\mu_{\delta}} \rangle$	$\langle \epsilon_{\mu_{\alpha*}} \rangle$	$\langle \epsilon_{\mu_{\delta}} \rangle$	
		mas yr ⁻¹						
1	GPS (Gaia+PS1+SDSS+2MASS)	1.74±0.54	1.53±0.46	1.35±0.33	1.21±0.29	1.89±0.51	1.72±0.48	50000
2	GP (Gaia+PS1+2MASS)	1.67±0.52	1.45±0.51	1.41±0.41	1.23±0.35	2.59±1.11	2.20±0.96	50000
3	PD (PS1+SDSS+2MASS)	3.00±1.01	2.60±1.02	1.91±0.48	1.72±0.45	2.65±0.85	2.44±0.79	50000
4	PS1 (<i>only</i> PS1)	4.34±2.55	3.51±2.05	2.53±0.90	2.12±0.73	4.58±2.33	3.75±1.88	50000

^a The uncertainties of the proper motions in $14 < m_r < 18$ are marked by black dashed lines in Figure 7.

^b We randomly select 50,000 objects from across the sky to derive these statistics. The proper motion estimates from the GPS, PS, and PS1 modes are provided for each star in the GPS1 catalog. So, the analysis for these three cases is based on the same sample taken from within the SDSS. Only the objects in the non-SDSS regions have proper motion estimates using only GP. Therefore, the statistics for the GP mode in the table are derived from a sample outside the SDSS coverage.

tions in the PS1 mode by $\sim 1.6 \text{ mas yr}^{-1}$ individually, and by $\sim 2.0 \text{ mas yr}^{-1}$ together. Therefore, Gaia and SDSS are comparably important for reducing uncertainties for the faint stars.

For stars with $14 < m_r < 18$, the GPS1 catalog is at its best. Photon noise matters little, yet the sources are not saturated. Figure 8 illustrates the distribution of uncertainties of these stars as Mollweide projection maps of the entire 3π region of the sky in equatorial coordinate system, containing six million stars randomly selected. The median uncertainty in each pixel is calculated from hundreds of stars. The median values of the uncertainties are $\sim 1.5 \text{ mas yr}^{-1}$ for both μ_{α^*} (the left panel) and μ_δ (the right panel), as shown in the maps. The uncertainties at high and low declinations are larger, as SDSS data missing. The small uncertainties in the north Galactic cap are driven by the SDSS observations taken ten or fifteen years ago.

Figure 9 shows the distribution of reduced χ^2 for the proper motion fit for a random subset of stars. This suggests that the proper motions are well fit for most of the stars, and that perhaps the individual uncertainty estimates are somewhat conservative. The actual uncertainties may be slightly smaller than our estimates.

4.2. Validation of Proper Motions

We now turn to the astrophysical validation of the derived proper motions, using galaxies, QSOs, distant stars and star clusters with well-known proper motions. All these validations have issues that require attention: galaxies and QSOs are distant enough to know *a priori* that their proper motions can be neglected; but galaxies are extended and often asymmetric objects, and QSOs with their strong emission lines show peculiar differential chromatic refraction (DCR). Stars in the Galactic halo are simple point sources, but may not be distant enough to have negligible proper motion: in particular, reflex of the Sun's motion is still observable up to 30 kpc. Member stars of open clusters share a common motion, but non-member contamination may be difficult to remove. Sources bright enough to have TGAS proper motions are too bright to be in the present sample. Therefore, there is no simple, ideal set of astrophysical sources to easily validate our proper motion estimates.

4.2.1. Validation with Galaxies

We select a sample of galaxies from the region covered by the PS1, SDSS, and Gaia surveys, and calculate the proper motions in two data combinations: PS1 and GPS modes. Figure 10 shows that the median of these apparent (and presumably spurious) proper motions lies within $\pm 0.3 \text{ mas yr}^{-1}$ of zero, implying that the accuracy of proper motion is better than 0.3 mas yr^{-1} . It also implies that this is a consistency check, since we used galaxies to build the reference frame, the proper motions of galaxies should be zero by design. The actual precision for galaxies is of course worse than that for stars, as they are extended.

4.2.2. Validation with QSOs

Hernitschek et al. (2016) identified a sample of over a million QSO candidates from the PS1 3π survey image data. QSOs have strong emission lines, which cause subtle image centroid effects, when differential chromatic refraction (DCR) comes into play. For validation, we only choose QSOs with high probability in $14.0 < m_r < 17.5$.

Figure 11 displays the apparent (and spurious, if significantly non-zero) proper motion distributions of the QSOs,

showing the entire PS1 3π sky region in an equatorial Mollweide projection. The median value in each pixel is calculated using QSOs that lie within a radius of 10° , a size that ensures inclusion of at least tens of QSOs. The apparent proper motions of QSOs show a significant non-zero pattern across the sky especially in δ . At high declinations, the δ proper motions are biased by up to 2 mas yr^{-1} . At low declinations, the δ proper motions are slightly under-estimated by $\sim 0.5 \text{ mas yr}^{-1}$. For comparison, Figure 12 displays the apparent proper motions measured when only fitting the PS1 Season-AVG points. Similar to Figure 11, the δ proper motions (the right panel) in high and low declinations are also over- and under-estimated by an average of $\sim 0.5 \text{ mas yr}^{-1}$, respectively. There is an obvious pattern in the region of $170^\circ < \alpha < 220^\circ$ and $-20^\circ < \delta < 20^\circ$ at the map of α proper motions (the left panel). It is probably caused by the PS1 observation, since the pattern looks even clearer than that in the GPS1 proper motion map (the left panel in Figure 11). We will discuss the bias induced by DCR in Section 5.2.

4.2.3. Validation with Star Clusters

M67 is a well known open cluster with a distance of $\sim 850 \text{ pc}$. Given its well-defined main sequence track, member candidates of the cluster can be easily identified using a color-magnitude diagram (CMD). All member stars should have mutually indistinguishable proper motions, as the cluster has an internal velocity dispersion of $\sim 1 \text{ kms}^{-1}$ (Geller et al. 2015). Because we know the absolute proper motions of a few M67 members from TGAS (Gaia Collaboration et al. 2016a), M67 could be an ideal testbed for our proper motion accuracy. But this requires careful accounting of field star contamination.

Figure 13 presents a color ($g-i$) and magnitude (i -band) diagram, based on PS1 photometry of stars within an angular radius $r_2 = 1.03^\circ$ of M67 (see Kharchenko et al. 2012). The solid pink curve corresponds to the PARSEC synthetic stellar track built with the Padova web-server CMD 2.8¹, while the two dashed curves offset by $\pm 0.1 \text{ mag}$ define the region we use to select likely members. We select member candidates by three criteria: (1) $r < r_2$; (2) distributed between the two dashed lines in the CMD (see Figure 13); (3) $13.5 < m_r < 18.0$.

Most member stars are located within r_2 , but field stars might still significantly contaminate the membership in this region ($r < r_2$). Outside r_2 , the distribution is probably dominated by field contamination. Figure 14 shows the normalized Gaussian-kernel-Smoothed probability distribution of proper motions of the stars in the field of M67. The size of the Kernel was chosen to match the precision of the proper motions (2 mas yr^{-1}). The solid curves show the distribution (ψ_{m+f}) of the member candidates selected according to CMD, which are composed of both member and field stars. The dashed curves show the distribution (ψ_f) of stars within $r_2 < r < 2r_2$, which is dominated by field stars. The error bars are obtained using 100 bootstrap sub-samples.

To estimate the mean proper motion of the star cluster, we use Markov Chain Monte Carlo (MCMC) simulation² to determine the most likely values of the five parameters: $(\langle \mu_{\alpha^*} \rangle, \langle \mu_\delta \rangle, \sigma_{\mu_{\alpha^*}}, \sigma_{\mu_\delta}) = (-10.54, -2.94, 3.16, 3.37) \text{ mas yr}^{-1}$, and $r_m = 54\%$, where r_m is the member fraction of all stars within r_2 .

¹ <http://stev.oapd.inaf.it/cgi-bin/cmd2.8>

² We use the `emcee` code to run the MCMC (Foreman-Mackey et al. 2013)

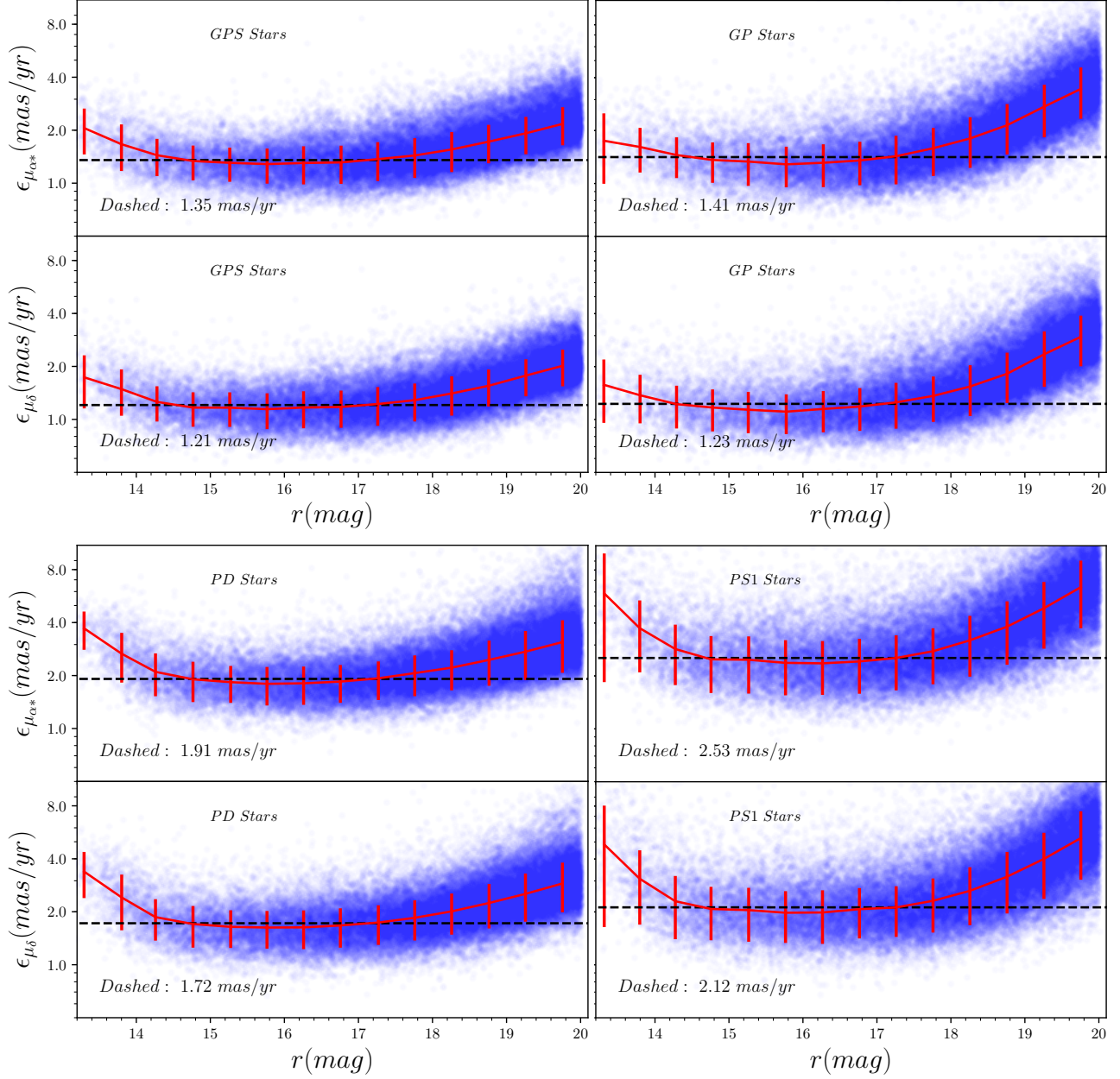


Figure 7. Proper motions precision for the four different combinations of data sets (top-left: GPS, top-right: GP, bottom-left: PS, and bottom-right: ONLY PS1). In the four panels, the red curves are the median uncertainties of proper motions within different magnitude bins, and the black lines mark typical average uncertainties in the magnitude range $14 < m_r < 18$. The blue scatter points represent the million stars randomly selected from the sky. All the uncertainties are logarithmic in every y-axis. The typical average uncertainties for the four combination modes are $\epsilon_{\mu_{\alpha^*}} \sim 1.35 \text{ mas yr}^{-1}$, $\epsilon_{\mu_{\delta}} \sim 1.21 \text{ mas yr}^{-1}$ for the GPS mode (top-left), $\epsilon_{\mu_{\alpha^*}} \sim 1.41 \text{ mas yr}^{-1}$, $\epsilon_{\mu_{\delta}} \sim 1.23 \text{ mas yr}^{-1}$ for the GP mode (top-right), $\epsilon_{\mu_{\alpha^*}} \sim 1.91 \text{ mas yr}^{-1}$, $\epsilon_{\mu_{\delta}} \sim 1.72 \text{ mas yr}^{-1}$ for the PD mode (bottom-left), and $\epsilon_{\mu_{\alpha^*}} \sim 2.53 \text{ mas yr}^{-1}$, $\epsilon_{\mu_{\delta}} \sim 2.12 \text{ mas yr}^{-1}$ for the ONLY PS1 mode (the bottom-right), respectively.

Within the angular radius of M67, we select two TGAS stars (see Table 4), whose proper motions are measured with high precision and the values are consistent with each other within errors. Also, their proper motions and parallaxes match those derived by Bellini et al. (2010). Therefore, their mean proper motion (-10.90 ± 0.12 , $-2.82 \pm 0.09 \text{ mas yr}^{-1}$) can be considered as a robust estimate of the proper motion of M67. For comparison, the mean GPS1 proper motion of the likely cluster members, $(\langle \epsilon_{\mu_{\alpha^*}} \rangle, \langle \epsilon_{\mu_{\delta}} \rangle) = (-10.54 \pm 0.14, -2.94 \pm 0.13) \text{ mas yr}^{-1}$ obtained from MCMC, is remarkably consistent with the robust estimate, as shown in Figure 15. This suggests that the GPS1 proper motions are measured not

only with a small random error, but also with a tiny systematic error.

We also compared our M67 proper motions with proper motions provided by PPMXL (Roeser et al. 2010) and UCAC4 (Zacharias et al. 2013) catalogs. Table 5 gives the proper motions of M67 estimated from four different catalogs. The value from TGAS is the robust estimate of the proper motion of M67, i.e., the average proper motion of two typical member stars listed in Table 4. Comparing with the robust value, the proper motion of GPS1 obtained from MCMC simulations shows a systematic offset of $< 0.3 \text{ mas yr}^{-1}$, almost 10 times better than PPMXL and UCAC4 ($> 2.0 \text{ mas yr}^{-1}$).

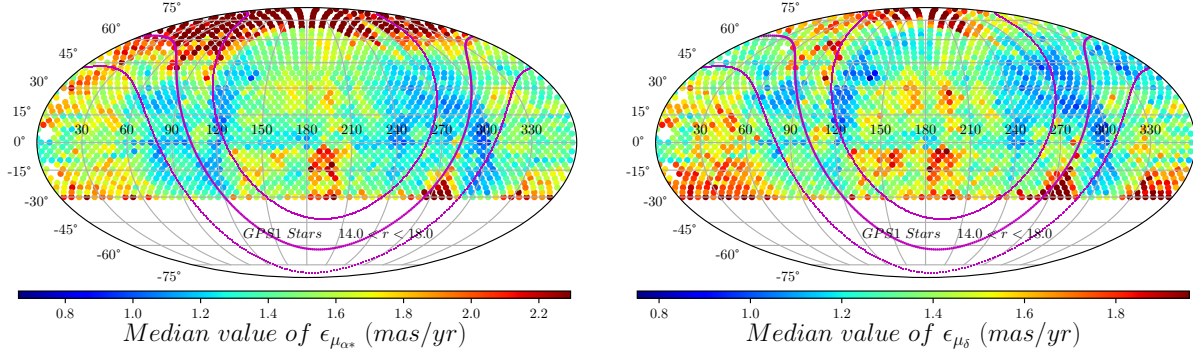


Figure 8. The distribution of proper motion uncertainties for stars with $14 < m_r < 18$; this is illustrated with an equatorial Mollweide projection of the entire 3π sky region. The pink solid ($b = 0^\circ$) and two dotted lines ($b = \pm 20^\circ$) mark the location of the Galactic plane in the equatorial coordinate system, where sources are crowded and the effects of dust extinction are manifest (Tian et al. 2014). To highlight the structures in the maps, the color bar is scaled in $\pm 3\sigma$ around the entire median value for each map.

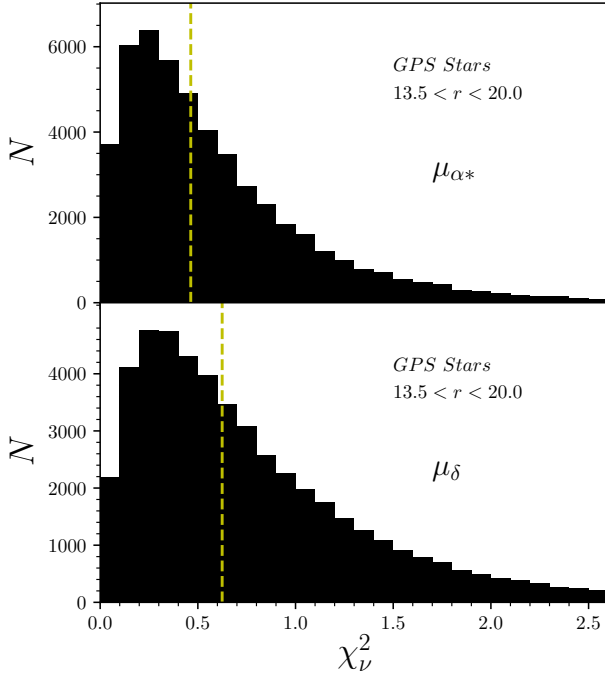


Figure 9. Illustration of the quality of the proper motion fits. Shown is the reduced χ^2 of the fits for the GPS case. The median values for both μ_{α^*} and μ_δ (marked with the yellow dashed lines) are smaller than 1, implying that most fits are good, and that the individual epochs' uncertainties are (slightly) conservative estimates.

Combining with Gaia DR1 data, Zacharias et al. (2017) and Altmann et al. (2017) recently updated the UCAC4 and PPMXL catalogs, and named the new catalogs UCAC5 and HSOY, respectively. Although the precisions of proper motions in the new catalogs are claimed to be improved to $1\text{--}5 \text{ mas yr}^{-1}$ with one year positions from Gaia DR1, the accuracies are not reported definitely in their papers. Fortunately, UCAC5 mainly focuses on the proper motions of bright sources ($r < 15 \text{ mag}$) with a precision of $< 2 \text{ mas yr}^{-1}$, which will fill up the gap in GPS1 catalog.

4.2.4. Proper motion validation using distant Galactic stars

We collect ~ 2200 distant stars ($d > 20 \text{ kpc}$) from the literature (Xue et al. 2008, 2014) with $13.5 < m_r < 17.5$, and calculate their proper motions. These distant halo stars roughly have zero mean velocity in the galactocentric frame and large

Table 4
TGAS Proper Motions for M67 Member Stars

ID	α	δ	$\mu_\alpha \cos(\delta)$	μ_δ	<i>parallax</i>	<i>g</i>
	deg		mas yr $^{-1}$		mas	mag
1	132.799	11.756	-10.86 ± 0.11	-2.82 ± 0.08	1.73 ± 0.55	10.04
2	132.875	11.788	-10.94 ± 0.13	-2.82 ± 0.10	1.03 ± 0.26	9.12

Table 5

The proper motions of M67 from the different catalogs

Catalog	$\mu_\alpha \cos(\delta)$	μ_δ
	mas yr $^{-1}$	
TGAS	-10.90 ± 0.12	-2.82 ± 0.09
GPS1	-10.54 ± 0.14	-2.94 ± 0.12
PPMXL	-7.20 ± 0.18	-5.80 ± 0.13
UCAC4	-9.00 ± 0.27	-5.10 ± 0.21

velocity dispersion, so they could be used for validation of GPS1 proper motions. But most stars in the sample are located in the range of $20 < d < 40 \text{ kpc}$, not distant enough for the Sun's reflex motion to be negligible. Therefore, we must correct for the Solar reflex motion before we use them for validation.

Figure 16 shows the histograms of the μ_{α^*} (the top panel) and μ_δ (the bottom panel), where we have adopted the solar motion as $(U_\odot, V_\odot, W_\odot) = (9.58, 10.52, 7.01) \text{ km s}^{-1}$ (Tian et al. 2015), and the IAU recommended circular speed of LSR as $v_0 = 220 \text{ km s}^{-1}$, to remove the solar reflex motion. The median values of the μ_{α^*} and μ_δ are $-0.14 \text{ mas yr}^{-1}$ and 0.13 mas yr^{-1} , and the dispersions are 2.33 mas yr^{-1} and 2.23 mas yr^{-1} , respectively. Accounting for this correction, the mean halo star proper motions are well within our accuracy estimate of 0.3 mas yr^{-1} .

The velocity dispersion of the halo stars widens the distribution of proper motions. Using the distances provided by Xue et al. (2008, 2014), one can calculate the median distance ($\sim 25 \text{ kpc}$) of this sample. Supposing the velocity dispersion in the halo is $\sim 100 \text{ km s}^{-1}$ (Deason et al. 2013), then the corresponding proper motion is around 0.85 mas yr^{-1} , which indicates that the true *rms* of the proper motion estimates is $\sim 2 \text{ mas yr}^{-1}$. This *rms* is slightly larger than 1.5 mas yr^{-1} as measured in Figure 7 and 8.

4.3. Comparison with other proper motions

Fritz & Kallivayalil (2015, hereafter, FK15) obtained high quality proper motion measurement of Palomar 5, using

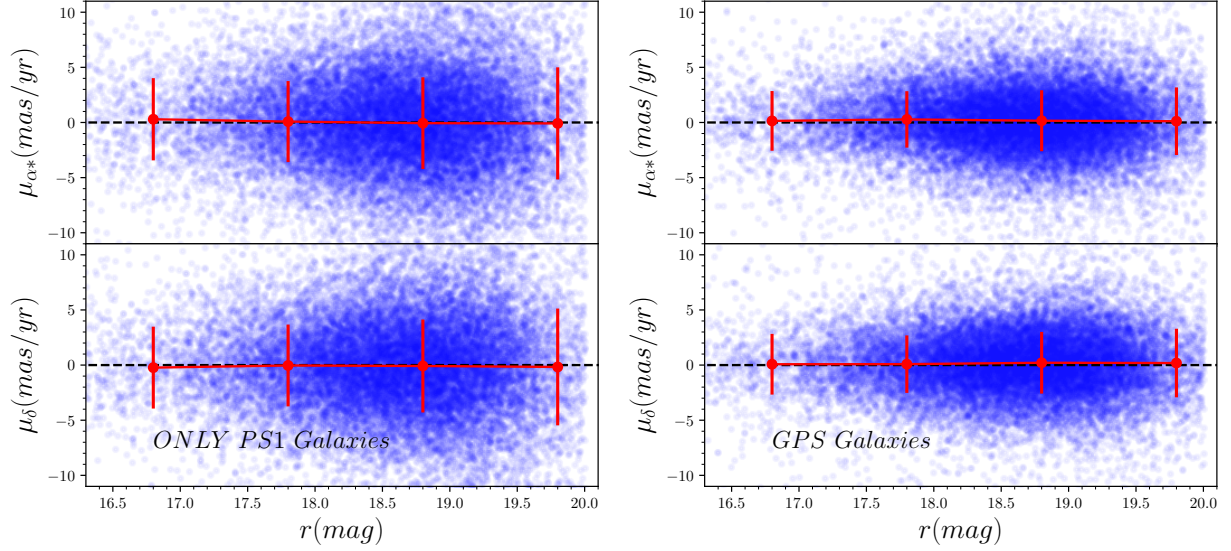


Figure 10. Validation of proper motions with galaxies in different magnitude bins. Two typical proper motions are presented: the PS1 proper motions (the left panel), and the GPS proper motions (the right panel). The red curves are the median values of proper motion in different magnitude bins and the error bars represent the robust rms . The black dashed lines mark zero proper motion. All the red points oscillate around the black dashed lines within $\pm 0.3 \text{ mas yr}^{-1}$ indicating that the accuracy of the proper motion is better than 0.3 mas yr^{-1} . The average rms in the ONLY PS1 case is $\sim 4.2 \text{ mas yr}^{-1}$, which is reduced to $\sim 2.8 \text{ mas yr}^{-1}$ in the GPS case.

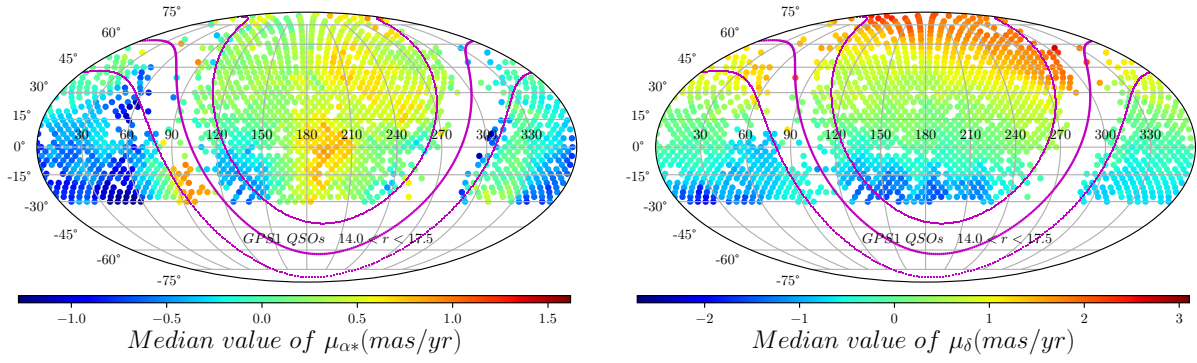


Figure 11. Validation of proper motions with QSOs in Mollweide projection map of the entire 3π sky region in the equatorial coordinate system. The pink solid ($b = 0^\circ$) and two dotted lines ($b = \pm 20^\circ$) represent the location of the Galactic plane in the equatorial coordinate system.

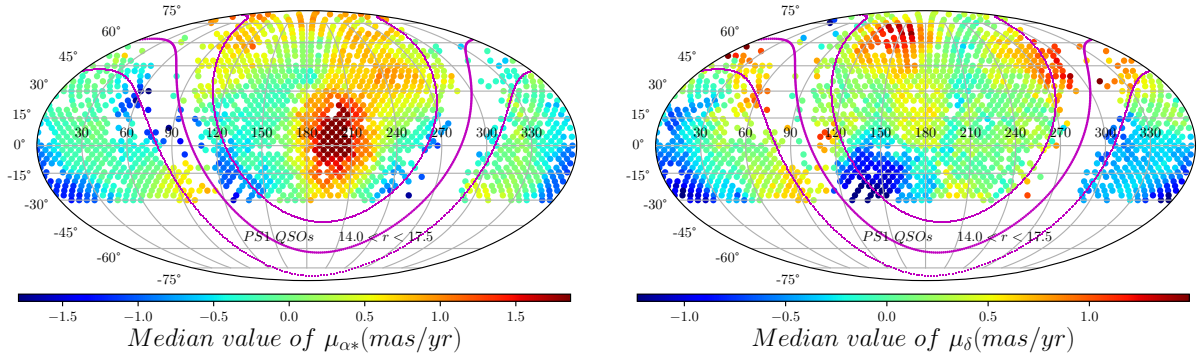


Figure 12. Same as Figure 11, but the proper motions of the QSOs in the maps are measured when only fitting PS1 SeasonAVG points.

SDSS and Large Binocular Camera (LBC) images. From the authors, we have obtained a proper motion sample of 1916 bright stars ($14.0 < m_r < 17.5$) in the field of Palomar 5. The proper motions show a wide range since most of the objects are field stars.

We then calculate the proper motions of stars in the same field, and cross-match the stars with the sample provided by

FK15. With the cross-matched 1887 stars, we compare our proper motions with different combinations, and also with PPMXL and UCAC4.

Figure 17 represents the comparison of proper motions between our GPS case and FK15 for μ_{α^*} (the left panel) and μ_{δ} (the right panel). The insets are the histograms of the error-weighted difference between the two, e.g. $\tilde{\Delta}\mu =$

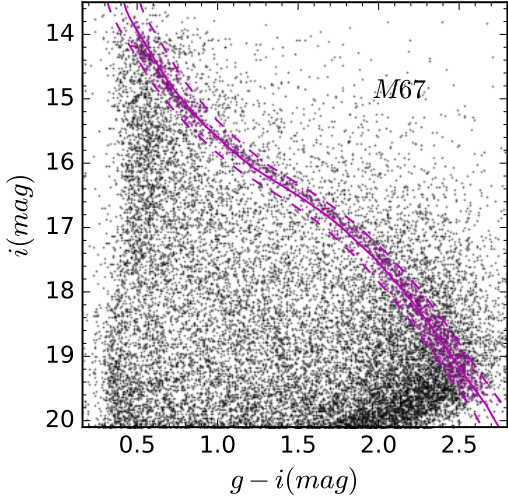


Figure 13. The color ($g-i$) and magnitude (i -band) diagram (CMD) of stars in the view field of M67, based on PS1 photometry. The pink solid curve in the CMD is the PARSEC synthetic stellar track, while the two dashed lines, offset by ± 0.1 mag serve for our photometric membership definition.

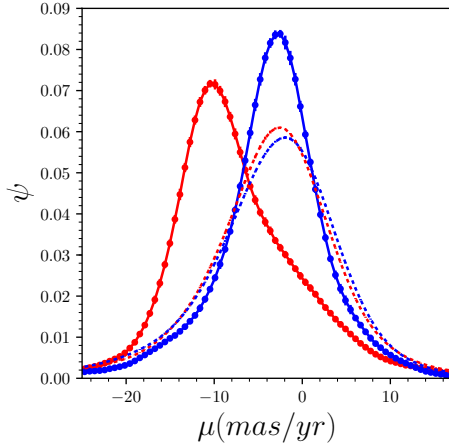


Figure 14. The normalized Gaussian-Kernel-Smoothed probability distribution of the proper motions (red for μ_{α^*} , blue for μ_{δ}) of the stars nearby M67. The solid curves are the distributions (ψ_{m+f}) of the member candidates which are composed by both the member and field stars within $r < r_2$. The dashed curves are the distribution (ψ_f) of the field stars within $r_2 < r < 2r_2$. The error bars are obtained from the 100 bootstrap sub-samples.

$(\mu_{ours} - \mu_{FK15}) / \sqrt{\epsilon_{\mu_{ours}}^2 + \epsilon_{\mu_{FK15}}^2}$, where the two ϵ are the errors of our and FK15 proper motions. The median of the error-weighted differences (marked by the white dashed lines) for the μ_{α^*} and μ_{δ} are -0.15 ± 1.27 and -0.42 ± 1.14 (the absolute values: -0.27 ± 2.27 mas yr $^{-1}$ and -0.80 ± 2.10 mas yr $^{-1}$), respectively. The plot shows that our proper motions are consistent with FK15 at the 1σ level. Note that their μ_{δ} estimates are higher by ~ 0.8 mas yr $^{-1}$ than ours, but the differences in μ_{α^*} are not notable. We also compared the proper motions from the GP, PS1, PPMXL and UCAC4 with FK15, and found that the μ_{α^*} are matched, just with much larger dispersions ($3.0 \sim 3.5$ mas yr $^{-1}$). But μ_{δ} from FK15 is also higher by ~ 1.0 mas yr $^{-1}$ than that from GP, PS1, PPMXL, and UCAC4.

5. GPS1 LIMITATIONS

For the most part, GPS1 should constitute a catalog that is far more accurate and considerably more precise than existing

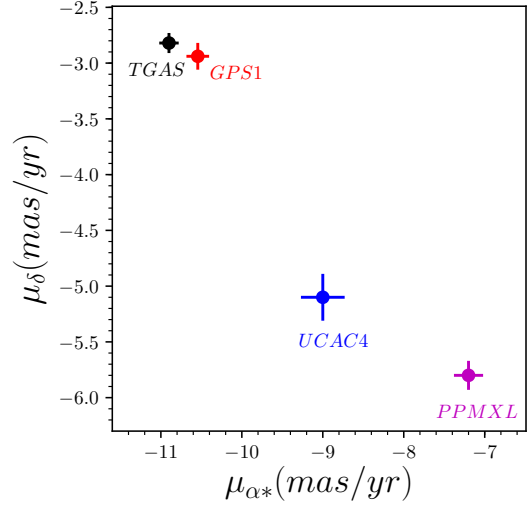


Figure 15. Validation of the GPS1 proper motion precision and accuracy, using the open cluster M67. The black point marks the median proper motion of the two member stars listed in Table 4. The red point is the mean proper motion obtained from MCMC. For comparison, the values from PPMXL (the pink point) and UCAC4 (the blue point) are also displayed in the panel.

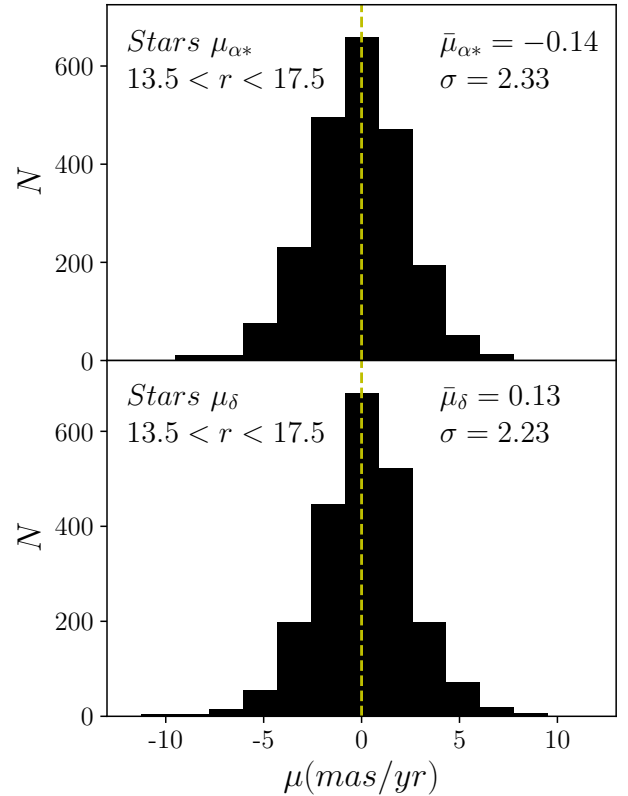


Figure 16. Validation of GPS1 proper motions with distant halo stars. The solar motion, $(U_{\odot}, V_{\odot}, W_{\odot}) = (9.58, 10.52, 7.01)$ km s $^{-1}$ (Tian et al. 2015), has been removed, assuming an azimuthal LSR velocity of $v_0 = 220$ km s $^{-1}$. The light dashed lines denote zero mas yr $^{-1}$, expected for a distant stellar halo of negligible rotation.

catalogs of comparable size and depth, PPMXL and UCAC4. In Section 4.2 we have described our catalog validation efforts. Here, we discuss a number of regimes, where GPS1 has limitations beyond its quoted uncertainties, and where it should be used with caution.

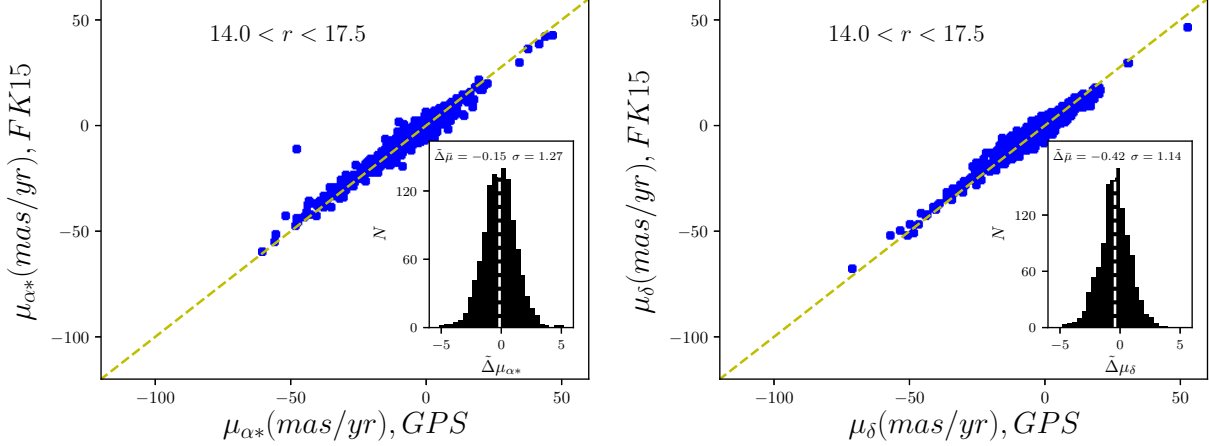


Figure 17. Comparison of proper motions between GPS and FK15 for μ_{α^*} (the left panel) and μ_{δ} (the right panel), based on stars near the Palomar 5. The insets are histograms of the error-weighted difference between our proper motion and FK15. The median of the error-weighted differences (the white dashed line) for the μ_{α^*} and μ_{δ} are -0.15 ± 1.27 and -0.42 ± 1.14 (the absolute values: $-0.27 \pm 2.27 \text{ mas yr}^{-1}$ and $-0.80 \pm 2.10 \text{ mas yr}^{-1}$), respectively. Note that the SDSS positions have been used in both proper motions estimates.

5.1. Proper Motions in Crowded regions

The reference frame calibration across the different surveys is difficult in crowded regions, for example near globular clusters, for two reasons: on the one hand, source crowding (the different surveys differ by a factor of ≥ 5 in resolution) may lead to systematic errors in source centering. On the other hand, blended sources may be classified erroneously as extended sources, which are then presumed to have zero proper motion. If that happens too often in crowded regions, the mean proper motion of the stellar sample may inevitably be driven towards zero by our calibration approach.

To explore these effects, we calibrated a sample of stars near the globular cluster M13, with two variants of bringing different epochs to the same reference frame. In one case we use objects classified as galaxies within the core radius. In the other, we do not. For these two cases, the final proper motions of stars close to the core region are significantly different. This indicates that misclassification of galaxies in a crowded core causes poor reference frame calibration. If stars are too close, i.e., if their angular distance is smaller than 1.5 mas, the procedure that associates repeatedly observed positions with unique objects, will fail for one of the stars in such a pair. The proper motion of such a star will thus be incorrect.

In order to reduce the impacts of crowding on positional calibration, we simply do not use the galaxies within the core radius of known globular clusters. We also use the bright galaxies in the Galactic plane to build a relatively reliable reference with PS1 for this study. In a future paper, Tian et. al. (*in preparation*) we plan a more complex calibration for stars in crowded regions with the aim of measuring proper motions for thousands of known star clusters and search for new star cluster candidates using the GPS1 catalog.

5.2. The impact of DCR

Refraction of the Earth's atmosphere varies with airmass and wavelength, resulting in differential chromatic refraction (DCR). Airmass depends on declination, right ascension, and the observational time and location of the observatory. For PS1, most observations are taken near meridian, so declination becomes a rough proxy for airmass.

The effect of DCR on QSOs is complex, due to their wide

emission lines and a large range in redshifts (Kaczmarczik et al. 2009). Moreover, Gaia, PS1 and SDSS surveys were conducted under different conditions: Gaia is a space-based telescope, and its observations are not affected by DCR; while PS1 and SDSS are ground-based telescopes and located in different places, so the two surveys suffer from DCR to a different extent. The combination of different surveys in the proper motion fit may lead to complex DCR effects. In order to figure out how the DCR affects the proper motions, we choose three samples of QSOs and stars in three declinations, and divide them into different magnitude bins. Figure 18 displays the magnitude and declination dependent impact of DCR (reflected in non-zero proper motions) on QSOs in the left panel and on stars in the right panel.

For QSOs in the PS1 case, the observations near the meridian greatly reduce the impact of DCR on μ_{α^*} (top-left, dashed lines). The deviation from zero (dot black line) is only $\sim -0.2(+0.2) \text{ mas yr}^{-1}$ in the low (high) declinations, particularly in the bins with $m_r > 17.5$. However, the impact on μ_{δ} is much more pronounced (bottom-left, dashed lines), the deviation is $\sim -0.5(+0.5) \text{ mas yr}^{-1}$ in the low (high) declination. The tendency of under (over) estimation of μ_{δ} in the low (high) declination increases as towards faint end. In the GPS case (solid lines), the impact of DCR on μ_{δ} (bottom-left) turns to be worse. The under (over) estimation can be up to $\sim -4.0(+4.0) \text{ mas yr}^{-1}$ in the low (high) declination, and the trends of the deviation from zero are almost same as the case in PS1. Gaia and SDSS detections, even if they were more "correct" than the PS1 measurements, apparently amplify the effect of DCR.

For stars we can still explore how the inclusion of Gaia and SDSS data affect the proper motion estimates, compared to PS1 only. We do this by analyzing the proper motion estimate differences, for example, $\mu_{GPS} - \mu_{PS1}$ (solid curves) and $\mu_{PD} - \mu_{PS1}$ (dashed curves), shown in the right panel of Figure 18. The difference between GPS and PS1 is very small ($\Delta\mu_{\alpha} < 0.2 \text{ mas yr}^{-1}$, $\Delta\mu_{\delta} < 0.5 \text{ mas yr}^{-1}$) for both μ_{α^*} (top-right) and μ_{δ} (bottom-right) except in the bin of bright stars where the star number is small. It indicates that Gaia and SDSS do not amplify the DCR impacts on stars unlike QSOs. The dashed lines demonstrate that the SDSS detec-

tions change the inferred proper motions of PS1 significantly at high declinations. The shifts on μ_δ of PS1 caused by SDSS detections (bottom-right, red dashed curve) are linearly dependent on magnitude, and $\Delta\mu_\delta$ can deviate as much as $\sim -0.9 \text{ mas yr}^{-1}$. Interestingly, Gaia seems to replicate this kind of significant shifts caused by SDSS, as shown by the red solid curve in the bottom right panel.

We also investigate the case of galaxies, but do not detect any significant impacts due to DCR. The median proper motions of galaxies are around 0.0 mas yr^{-1} ($< 0.2 \text{ mas yr}^{-1}$), except at low declinations where they are non-zero ($< 0.5 \text{ mas yr}^{-1}$), as displayed in Figure 19.

In general, the DCR impacts the proper motions of QSO in a complex and noticeable manner. Therefore, QSOs are not ideal sources for the validation of proper motions, as discussed in Section 4.2.2. However, DCR has a more benign influence on stars and galaxies.

5.3. The origin of the magnitude and declination dependent offsets in predicted Gaia positions

In Section 3.2.2, we reported the positional offsets between the predicted, from PS1, and the originally observed Gaia positions. As shown in Figure 4, the positional offsets of stars are significantly dependent on magnitude and declination. Positions can have offsets of up to $\sim \pm 10 \text{ mas}$.

Magnier et al. (2017) point out that the position of PS1 sources depends on flux and may be affected by imperfect DCR corrections. Due to charge leakage, bright stars are offset on PS1 camera CCDs relative to faint stars. This leakage is stronger in the case of brighter stars. This effect was first identified by Koppenhöfer & Henning (2011). The DCR is a typical declination dependent effect that arises due to variation of airmass in the direction of declination for observations near meridian. The combined impact of the two effects might induce spurious proper motions from PS1, with which the predicted Gaia positions could be magnitude and declination dependent. Although these two systematic effects were corrected in Magnier et al. (2017), that correction may be imperfect.

6. CONCLUSIONS

The PS1, Gaia, SDSS, and 2MASS surveys have collected positions for billions of stars, with precise relative astrometry across a baseline of ~ 15 years. By combining them, we build a catalog of proper motions for ~ 350 million point sources brighter than $m_r \sim 20 \text{ mag}$, across three quarters of the sky. The systematic error (i.e. accuracy) is $< 0.3 \text{ mas yr}^{-1}$ and the typical uncertainty in the proper motion of a single source is $\sim 1.5 \text{ mas yr}^{-1}$ (for sources brighter than $m_r = 18$).

Our analysis required that the cataloged source positions of all surveys at all separate epochs be brought to a common reference frame. We accomplished this by requiring that galaxies have zero proper motion and that angular motions of stars on the sky are essentially linear. We verified that this approach leads to proper motion estimates of the precision and accuracy stated above. There are several important exceptions that we discuss, in particular QSOs and crowded fields.

We compare GPS1 with published large scale proper motion catalogs in Section 4.3: the accuracy of GPS1 ($< 0.3 \text{ mas yr}^{-1}$) is ~ 10 times better than PPMXL and UCAC4 ($> 2.0 \text{ mas yr}^{-1}$), and the precision ($\sim 1.5 \text{ mas yr}^{-1}$) is ~ 4 times better than PPMXL and UCAC4 ($\sim 6.0 \text{ mas yr}^{-1}$).

Until Gaia DR2, GPS1 should provide a valuable resource for kinematic studies of the Milky Way.

The authors thank Bin Yue, Andy Gould for the helpful discussions, and Tobias Fritz for providing the proper motions of stars in the field of Palomar 5. H.-J.T. acknowledges the National Natural Science Foundation of China (NSFC) under grants 11503012, U1331202 and the fellowships from China Scholarship Council (CSC) and Max Planck Institute for Astronomy. B.S. and H.-W.R. acknowledge funding from the European Research Council under the European Union's Seventh Framework Programme (FP 7) ERC Grant Agreement n. [321035]. B.G. acknowledge funding from Sonderforschungsbereich SFB 881 "The Milky Way System" (subproject A3 and B6) of the German Research Foundation (DFG). The Pan-STARRS1 Survey (PS1) has been made possible through contributions of the Institute for Astronomy at the University of Hawaii, Pan-STARRS Project Office, Max-Planck Society and its participating institutes, specifically Max Planck Institute for Astronomy, Heidelberg and Max Planck Institute for Extraterrestrial Physics, Garching, Johns Hopkins University, Durham University, University of Edinburgh, Queen's University Belfast, Harvard-Smithsonian Center for Astrophysics, Las Cumbres Observatory Global Telescope Network Incorporated, National Central University of Taiwan, Space Telescope Science Institute, National Aeronautics and Space Administration under Grant No. NNX08AR22G issued through the Planetary Science Division of the NASA Science Mission Directorate, the National Science Foundation under Grant No. AST-1238877, University of Maryland, Eotvos Lorand University and Los Alamos National Laboratory. This work has made use of data from the European Space Agency (ESA) mission *Gaia* (<https://www.cosmos.esa.int/gaia>), processed by the *Gaia* Data Processing and Analysis Consortium (DPAC, <https://www.cosmos.esa.int/web/gaia/dpac/consortium>). Funding for the DPAC has been provided by national institutions, in particular the institutions participating in the *Gaia* Multilateral Agreement.

REFERENCES

- Altmann, M., Roeser, S., et al. 2017, arXiv:1701.02629v2
 Bellini, A., Bedin, L. R., et al. 2010, A&A, 513, A51
 Calabretta, M. R., & Roukema, B. F. 2007, MNRAS, 381, 865
 Chambers, K. 2011, American Astronomical Society Meeting Abstracts #218, 113.01
 Chambers, K. C., Magnier, E. A., et al. 2016, arXiv:1612.05560
 Deason, A. J., Van der Marel, R. P., et al. 2013, ApJ, 766, 24
 de Bruijne, J. H. J. 2012, Ap&SS, 341, 31
 Eisenstein, D. J., Weinberg, D. H., et al. 2011, AJ, 142, 72
 Fedorov, P. N., Myznikov, A. A., & Akhmetov, V. S. 2009, MNRAS, 393, 133
 Fritz, T. K., Kallivayalil, N., 2015, ApJ, 811, 123 (FK15)
 Foreman-Mackey, D., Hogg, D. W., Lang, D., & Goodman, J. 2013, PASP, 125, 306
 Fukugita, M., Ichikawa, T., Gunn, J. E., et al. 1996, AJ, 111, 1748
 Brown, A. G. A., Vallenari, A., Makarov, V. V., et al. 2016, A&A, 595, A2
 Geller, A. M., Latham, D. W., Mathieu, R. D. 2015, AJ, 150, 97
 Gunn, J. E., Carr, M., Rockosi, C., et al. 1998, AJ, 116, 3040G
 Gunn, J. E., Siegmund, W. A., et al. 2006, AJ, 131, 2332
 Hernitschek, N., Schlafly, E. F., Sesar, B., et al. 2016, ApJ, 817, 73H
 Høg, E., Fabricius, C., Makarov, V. V., et al. 2000, A&A, 355, L27
 Juric, M. 2012, Astrophysics Source Code Library, record ascl:1209.003
 Kaczmarek, M. C., Richards, G. T., Mehta, S. S., & Schlegel, D. J. 2009, AJ, 138, 19
 Kharchenko, N. V., Piskunov, A. E., et al. 2012, A&A, 543, 156
 Koppenhöfer, J., Henning, T. 2011, American Astronomical Society Meeting Abstracts #218, 113.04
 Lindegren, L., Lammers, U., et al. 2016, A&A, 595, A4
 Liu, C., Tian, H. J., Wan, J.-C., et al. 2016, in prepare
 Lupton, R. 1993, Statistics in theory and practice, Princeton University Press
 Magnier, E. A., Liu, M., et al. 2008, IAU Symposium, Vol. 248, 553-559
 Magnier, E. A., Schlafly, E. F., et al. 2016, arXiv:1612.05242
 Michalik, D., Lindegren, L., & Hobbs, D. 2015, A&A, 574, 115
 Monet, D. G., Levine, S. E., Canzian, B., et al. 2003, AJ, 125, 984

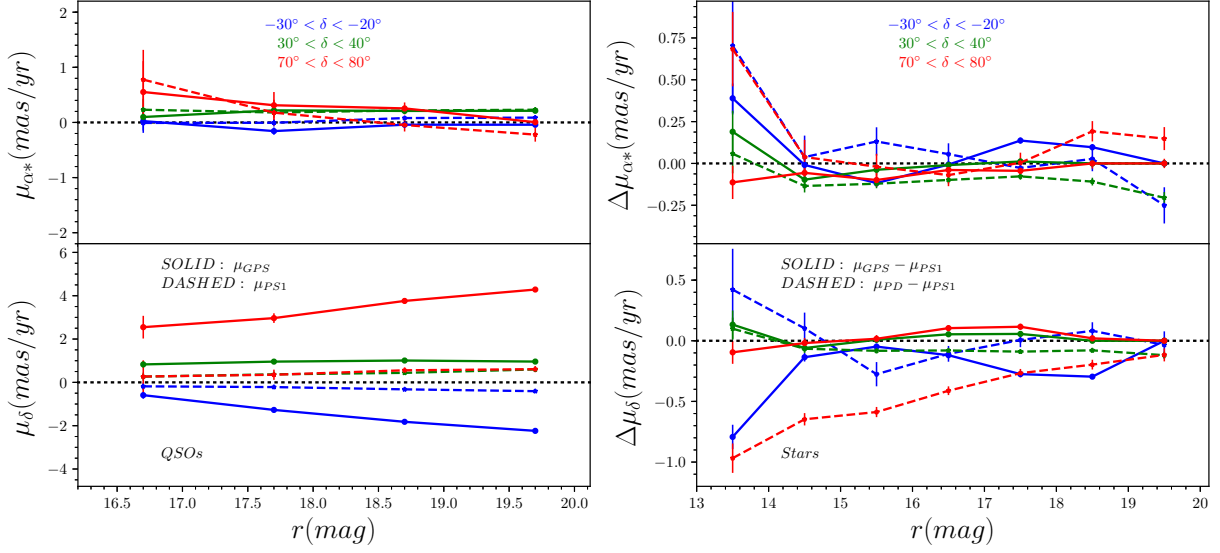


Figure 18. The magnitude dependent and declination dependent DCR impacts on QSOs (the left panel) and stars (the right panel). The solid (dashed) curves represent the proper motions in GPS (PS1) in the left panel, and the difference of proper motions between GPS (PD) and PS1 modes in the right panel. The different colors in both the panels depict the cases of different declinations (blue for low, green for intermediate and red for high), while the black dotted lines mark the zero-level.

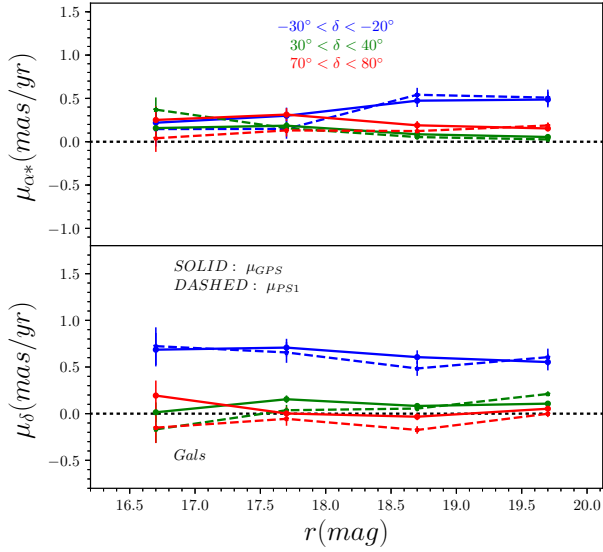


Figure 19. Same as Figure 18, but depicts the case of proper motions of galaxies in different magnitudes and declination bins. The median proper motions are $\sim 0 \text{ mas yr}^{-1}$ ($< 0.2 \text{ mas yr}^{-1}$), except in the low declination, where they are non-zero ($< 0.5 \text{ mas yr}^{-1}$).

- Munn, J. A., Monet, D. G., Levine, S. E., et al. 2004, *AJ*, 127, 3034
 Röser, S., Schilbach, E., et al. 2008, *A&A*, 488, 401
 Röser, S., Demleitner, M., & Schilbach, E. 2010, *ApJ*, 139, 2447
 Schlafly, E. F., Finkbeiner, D. F., et al. 2012, *ApJ*, 756, 158
 Schn, S. T., Besla, G., et al. 2013, *ApJ*, 768, 139
 Skrutskie, M. F., et al. 2006, *AJ*, 131, 1163
 Stoughton, C., et al. 2002, *AJ*, 123, 485
 Stubbs, C. W., Doherty, P., et al. 2010, *ApJS*, 191, 376
 Tian, H. J., Liu, C., Hu, J. Y., et al. 2014, *A&A*, 561, A142
 Tian, H. J., Liu, C., Carlin, J. L., et al. 2015, *ApJ*, 809, 145
 Tian, H. J., Liu, C., Wan, J.-C., et al. 2016, arXiv:1603.06262
 Tonry, C. W., Stubbs, K. R., et al. 2012, *ApJ*, 750, 99
 Vickers, J. J., Röser, S., & Grebel, K. E. 2016, *ApJ*, 151, 99
 Xue, X. X., Rix, H. W., Zhao, G., et al. 2008, *ApJ*, 684, 1143
 Xue, X. X., Ma, Z. B., Rix, H. W., et al. 2014, *ApJ*, 784, 170
 York, D. G., Adelman, J., et al. 2000, *AJ*, 120, 1579
 Zacharias, N., Finch, C. T., Girard, T. M., et al. 2013, *AJ*, 145, 44
 Zacharias, N., Finch, C., Girard, T., et al. 2010, *AJ*, 139, 2184
 Zacharias, N., Urban, S. E., Zacharias, M. I., et al. 2004, *AJ*, 127, 3043
 Zacharias, N., Finch, C., & Frouard, J. 2017, arXiv:1702.05621v1